

# Chasing the Tail of Cosmic Reionization with Dark Gap Statistics in the Ly $\alpha$ Forest over 5 < z < 6

Yongda Zhu<sup>1</sup>, George D. Becker<sup>1</sup>, Sarah E. I. Bosman<sup>2</sup>, Laura C. Keating<sup>3</sup>, Holly M. Christenson<sup>1</sup>, Eduardo Bañados<sup>2</sup>, Fuyan Bian<sup>4</sup>, Frederick B. Davies<sup>2</sup>, Valentina D'Odorico<sup>5,6,7</sup>, Anna-Christina Eilers<sup>8,14</sup>, Xiaohui Fan<sup>9</sup>, Martin G. Haehnelt<sup>10</sup>, Girish Kulkarni<sup>11</sup>, Andrea Pallottini<sup>6</sup>, Yuxiang Qin<sup>12,13</sup>, Feige Wang<sup>9,14</sup>, and Jinyi Yang<sup>9,15</sup>

<sup>2</sup> Max-Planck-Institut für Astronomie, Königstuhl 17, D-69117 Heidelberg, Germany

<sup>3</sup> Leibniz-Institut für Astrophysik Potsdam (AIP), An der Sternwarte 16, D-14482 Potsdam, Germany

<sup>4</sup> European Southern Observatory, Alonso de Córdova 3107, Casilla 19001, Vitacura, Santiago 19, Chile

<sup>5</sup> INAF-Osservatorio Astronomico di Trieste, Via Tiepolo 11, I-34143 Trieste, Italy

<sup>6</sup> Scuola Normale Superiore, Piazza dei Cavalieri 7, I-56126 Pisa, Italy

<sup>7</sup> IFPU—Institute for Fundamental Physics of the Universe, Via Beirut 2, I-34151 Trieste, Italy

<sup>8</sup> MIT Kavli Institute for Astrophysics and Space Research, 77 Massachusetts Avenue, Cambridge, MA 02139, USA

<sup>9</sup> Steward Observatory, University of Arizona, 933 North Cherry Avenue, Tucson, AZ 85721, USA

<sup>10</sup> Kavli Institute for Cosmology and Institute of Astronomy, Madingley Road, Cambridge, CB3 0HA, UK

<sup>11</sup> Tata Institute of Fundamental Research, Homi Bhabha Road, Mumbai 400005, India

<sup>12</sup> School of Physics, University of Melbourne, Parkville, VIC 3010, Australia

<sup>13</sup> ARC Centre of Excellence for All Sky Astrophysics in 3 Dimensions (ASTRO 3D), Australia

Received 2021 July 26; revised 2021 September 8; accepted 2021 September 13; published 2021 December 23

#### Abstract

We present a new investigation of the intergalactic medium (IGM) near the end of reionization using "dark gaps" in the Ly $\alpha$  forest. Using spectra of 55 QSOs at  $z_{\rm em} > 5.5$ , including new data from the XQR-30 VLT Large Programme, we identify gaps in the Ly $\alpha$  forest where the transmission averaged over 1 comoving  $h^{-1}$  Mpc bins falls below 5%. Nine ultralong ( $L > 80 h^{-1}$  Mpc) dark gaps are identified at z < 6. In addition, we quantify the fraction of QSO spectra exhibiting gaps longer than  $30 h^{-1}$  Mpc,  $F_{30}$ , as a function of redshift. We measure  $F_{30} \simeq 0.9$ , 0.6, and 0.15 at z = 6.0, 5.8, and 5.6, respectively, with the last of these long dark gaps persisting down to  $z \simeq 5.3$ . Comparing our results with predictions from hydrodynamical simulations, we find that the data are consistent with models wherein reionization extends significantly below redshift six. Models wherein the IGM is essentially fully reionized that retain large-scale fluctuations in the ionizing UV background at  $z \lesssim 6$  are also potentially consistent with the data. Overall, our results suggest that signatures of reionization in the form of islands of neutral hydrogen and/or large-scale fluctuations in the ionizing background remain present in the IGM until at least  $z \simeq 5.3$ .

*Unified Astronomy Thesaurus concepts*: Reionization (1383); Intergalactic medium (813); Quasar absorption line spectroscopy (1317); High-redshift galaxies (734)

Supporting material: Data behind figure, figure set, machine-readable table

# 1. Introduction

The reionization of the intergalactic medium (IGM) is the last major phase transition in the history of the universe. In the widely accepted picture, neutral hydrogen in the IGM was reionized by ultraviolet photons emitted by the first luminous sources (e.g., Bromm & Larson 2004; McQuinn 2016; Dayal & Ferrara 2018). Determining when reionization occurred as well as what sources were responsible is therefore important for understanding the formation and evolution of the first stars, galaxies, and black holes.

Multiple observations now constrain the timing of reionization. Cosmic microwave background (CMB) measurements suggest a midpoint at redshift  $z_{\rm re}=7.7\pm0.7$  (Planck Collaboration et al. 2020; see also de Belsunce et al. 2021). The redshift evolution in the fraction of UV-selected galaxies detected in Ly $\alpha$  emission also suggests that the IGM was significantly neutral near  $z\sim7-8$  (e.g., Mason et al. 2018, 2019; Hoag et al. 2019; Hu et al. 2019, and references

therein, but see Jung et al. 2020 and Wold et al. 2021). These results are broadly consistent with multiple probes of the IGM using QSO spectra. For example, the IGM thermal history at z > 4 inferred from the Ly $\alpha$  flux power spectrum suggests a mean redshift of reionization near  $z_{\rm re} \simeq 8.5^{+1.1}_{-0.8}$  (Boera et al. 2019, see also Walther et al. 2019; Gaikwad et al. 2021). Similarly, Ly $\alpha$  damping wing measurements of  $z_{\rm em} > 7$  QSOs indicate that the IGM was significantly neutral at  $z \sim 7-7.5$ (e.g., Bañados et al. 2018; Davies et al. 2018a; Greig et al. 2017, 2019; Wang et al. 2020; Yang et al. 2020a). The appearance of transmitted flux in the Ly $\alpha$  and Ly $\beta$  forests suggests that reionization was mostly completed by  $z \simeq 6$  (e.g., McGreer et al. 2015). On the other hand, large fluctuations in the observed IGM effective opacity ( $\tau_{\rm eff} = -\ln \langle F \rangle$ , where F is the continuum-normalized flux) in the Ly $\alpha$  forest at z < 6suggest that signatures of reionization may persist in the IGM down to even lower redshifts (Fan et al. 2006; Becker et al. 2015; Bosman et al. 2018; Eilers et al. 2018; Yang et al. 2020b; Bosman et al. 2021a).

Multiple models have been proposed to explain the largescale fluctuations in IGM Ly $\alpha$  opacity at z < 6. If the IGM is

<sup>14</sup> NASA Hubble Fellow.

<sup>15</sup> Strittmatter Fellow.

mostly ionized at  $z \ge 6$ , then large variations in Ly $\alpha$  opacity may persist to lower redshifts due to either lingering temperature fluctuations produced by inhomogeneous reionization (D'Aloisio et al. 2015), or fluctuations in the ionizing UV background produced by a short and spatially variable mean free path (Davies & Furlanetto 2016; Nasir & D'Aloisio 2020), or rare sources such as QSOs (Chardin et al. 2017; see also Meiksin 2020). Alternatively, if reionization continues substantially to z < 6, then the observed scatter in  $\tau_{\rm eff}$  could be due to the presence of large patches of neutral gas coupled with UVB fluctuations (e.g., Kulkarni et al. 2019a; Keating et al. 2020a; Nasir & D'Aloisio 2020; Qin et al. 2021). The combination of neutral patches and UVB fluctuations may naturally explain the presence of giant Ly $\alpha$  troughs, such as the  $110h^{-1}$  Mpc trough toward ULAS J0148+0600 identified by Becker et al. (2015) (e.g., Keating et al. 2020b). A late-ending reionization 16 scenario is also consistent with the evolution of O I absorbers at  $z \simeq 6$  (Becker et al. 2019), and is preferred by recent Bayesian inference results that simultaneously match Ly $\alpha$  forest, CMB, and galaxy data (Choudhury et al. 2021; Qin et al. 2021).

Some progress has been made toward distinguishing between these models observationally. Measurements of Ly $\alpha$ -emitting galaxies (LAEs, Becker et al. 2018, Christenson et al. 2021) and Lyman break galaxies (LBGs; Kashino et al. 2020) in the field of ULAS J0148+0600 have demonstrated that the Ly $\alpha$  trough along this line of sight is associated with a large-scale underdensity. This result disfavors the temperature fluctuation model, but is consistent with either the pure UVB fluctuation or late reionization model. The QSO UVB model is potentially also consistent with this result, though it is disfavored by measurements of the QSO luminosity function near  $z \sim 6$  (e.g., Parsa et al. 2018; Kulkarni et al. 2019b). Recent measurements of the mean free path of ionizing photons over 5 < z < 6 are consistent with late reionization models wherein the IGM is still significantly neutral at z = 6, and disfavor models in which reionization ends early enough that the IGM relaxes hydrodynamically by z = 6 (Becker et al. 2021). Simultaneously matching the mean free path measurements and other IGM constraints further favors a late and rapid reionization scenario, driven by galaxies that are efficient at producing and/or emitting ionizing photons (Cain et al. 2021; Davies et al. 2021).

A key question, therefore, is whether and for how long the impacts of reionization continued below z=6. It is also of interest to determine whether a late reionization scenario with islands of neutral gas and UVB fluctuations at z<6 can be distinguished observationally from an early reionization scenario with UVB fluctuations alone. Better measurements of the spatial scale of the Ly $\alpha$  opacity fluctuations may provide some insights. Determining how long these fluctuations persist and how they evolve with redshift may also be helpful. One way to do this is by identifying individual "dark gaps" in the Ly $\alpha$  forest (e.g., Songaila & Cowie 2002; Furlanetto et al. 2004; Paschos & Norman 2005; Fan et al. 2006; Gallerani et al. 2008, Gnedin et al. 2017), which could be created by regions of neutral IGM and/or low UV background (e.g., Nasir & D'Aloisio 2020). Because dark gaps contain multiscale spatial

information, they provide complementary information to  $\tau_{\rm eff}$  measurements averaged over intervals of fixed length, and may therefore be useful for distinguishing between models of the IGM at z < 6.

In this paper, we use dark gap statistics to characterize the opacity of the IGM over  $5\lesssim z\lesssim 6$ . In particular, we use these statistics to determine how long large Ly $\alpha$ -opaque regions persist in the IGM and whether the data are consistent with existing late reionization models and/or early reionization models that retain a fluctuating UVB. We use a sample of 55 high signal-to-noise (S/N) spectra of QSOs at  $5.5\lesssim z_{\rm em}\lesssim 6.5$ , including 23 new X-Shooter spectra from the XQR-30 VLT Large Programme (V. D'Odorico et al., in preparation). In addition to the distribution of dark gap lengths, we measure the fraction of QSO spectra exhibiting long  $(L\geqslant 30h^{-1}\,{\rm Mpc})$  dark gaps as a function of redshift for the first time.

We present our data in Section 2. In Section 3, we describe our methods for measuring dark gaps and the results of dark gap statistics. Section 4 introduces the models to which we compare our measurements. We then discuss the implications for the models in Section 5. Finally, we summarize our conclusions in Section 6. Throughout this paper we quote distances in comoving units unless otherwise noted, and assume a  $\Lambda$ CDM cosmology with h=0.678,  $\Omega_m=0.308$  and  $\Omega_{\Lambda}=0.692$ .

#### 2. The Data

# 2.1. QSO Spectra

This study is based on spectra of 55 QSOs at  $5.5 \lesssim z_{\rm em} \lesssim 6.5$ taken with the X-Shooter spectrograph on the Very Large Telescope (VLT; Vernet et al. 2011) and the Echellette Spectrograph and Imager (ESI) on Keck (Sheinis et al. 2002). Of these, 23 X-Shooter spectra are from the XQR-30 VLT Large Programme. The XQR-30 program is targeting 30 bright QSOs at  $5.8 \le z \le 6.6$  for the study of reionization and other aspects of the early Universe. The full data set will be described in V. D'Odorico et al. (in preparation). The 23 objects out of the XQR-30 sample selected for this project are those that meet our S/N threshold and do not contain strong BAL features. In addition, we use 30 spectra reduced from archival X-Shooter and ESI data, of which 27 are from the sample of Becker et al. (2019). Recent deep (20 hr) X-Shooter observations (PI: Fuyan Bian) of the lensed z = 6.5 QSO J0439 +1634 are also included in the dark gaps statistics. Finally, we acquired a deep (7 hr) ESI spectrum of SDSS J1250+3130. Observations for all objects except SDSS J1250+3130 were taken without any foreknowledge of dark gaps in the Ly $\alpha$ forest. In the case of SDSS J1250+3130, we targeted the QSO based on indications from a shallower (1 hr) ESI spectrum that its spectrum contained a long dark gap in the Ly $\alpha$  forest. We discuss the impact of including this object on our results in Section 3.4.

Details of the data reduction are given in Becker et al. (2019). Briefly, we used a custom pipeline that includes optimal techniques for sky subtraction (Kelson 2003) and one-dimensional spectral extraction (Horne 1986). Telluric absorption corrections were computed for individual exposures using models based on the Cerro Paranal Advanced Sky Model (Noll et al. 2012; Jones et al. 2013). The spectra were extracted using 10 km s<sup>-1</sup> pixels for the VIS arm of X-Shooter and 15 km s<sup>-1</sup> pixels for ESI. Typical resolutions for the X-Shooter and ESI

 $<sup>\</sup>overline{16}$  Throughout this paper, for convenience, we refer to "the end of reionization" as when the volume-filling factor of ionized gas in the IGM reaches 99%. We use "early" for scenarios wherein reionization ends at  $z \geqslant 6$ , and "late" for cases where reionization ends below z = 6.

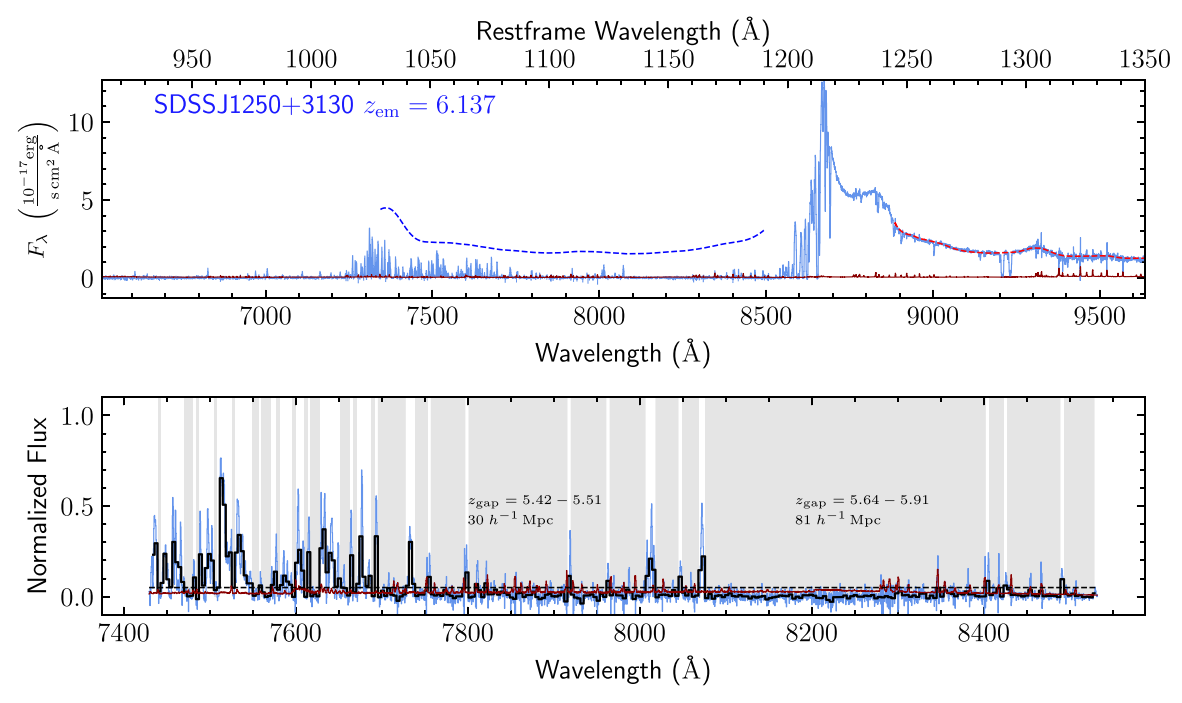


Figure 1. Spectrum, continuum fits, and dark gap detection details of the  $z_{\rm em}=6.137$  quasar SDSS J1250+3130. Top panel: QSO spectrum and continuum fits. The light blue and dark red lines represents flux and flux error in the original binning. Dashed red and blue curves are the best-fitting QSO continuum based on PCA. Bottom panel: Ly $\alpha$  forest and dark gaps detected. The dashed black line labels the flux threshold of 0.05. The thick black line displays the flux binned to  $1h^{-1}$  Mpc. Light blue and dark red lines show the flux and flux error in the original binning. Dark gaps detected are shaded with gray. We also label the redshift range and length of each long dark gap ( $L \ge 30h^{-1}$  Mpc), if any.

(The complete figure set (55 images) is available.)

are FWHM  $\approx 25 \, \mathrm{km \, s^{-1}}$  and 45 km s<sup>-1</sup>, respectively. In addition, for J0439+1634, to reduce the contamination from continuum emission of a foreground galaxy, we fit a power law of the flux zero-point over the Ly $\alpha$  forest and subtract it from the flux. The spectra are plotted in Figure 1.

We adopt QSO redshifts measured from CO, [C II] 158  $\mu$ m, or Mg II lines if available. Otherwise we use redshifts inferred from the apparent start of the Ly $\alpha$  forest, following Becker et al. (2019). Table 1 summarizes QSO spectra used in this work with the QSO redshifts, instruments, and estimated signal-to-noise ratios, which is calculated as the median ratio of unabsorbed QSO continuum to noise per 30 km s<sup>-1</sup> near 1285 Å in the rest frame.

# 2.2. Continuum Fitting

The detection of dark gaps relies on the construction of the intrinsic continuum over the Ly $\alpha$  forest. In order to estimate QSO continua blueward of the Ly $\alpha$  emission line, we use Principal Component Analysis (PCA), which is less biased than the conventional power-law fitting (e.g., Bosman et al. 2021b). In this work, we apply the log-PCA method of Davies et al. (2018b) as implemented in the Ly $\alpha$  forest portion of the spectrum by Bosman et al. (2021a), with 15 and 10 components used for the red-side (rest-frame wavelength  $\lambda_0 > 1230$  Å) and blue-side ( $\lambda_0 < 1170$  Å) continua, respectively. For each QSO, we fit the red-side continuum with principal components, and map the corresponding red principal component coefficients to the blue side coefficients with a projection matrix. For X-Shooter spectra with observations from the NIR arm, we fit the red continuum over  $1230 < \lambda < 2000$  Å in the rest frame.

The ESI spectra are fitted using an optical-only PCA, which is presented in Bosman et al. (2021b). QSOs with strong broad absorption lines (BALs) in their spectra were excluded from our sample. For OSOs with mild absorption features that interfere minimally with the Ly $\alpha$  forest, we mask out the absorption lines when fitting their spectra. In addition, we intentionally leave out the Ly $\alpha$  emission peak and the proximity zone when fitting and predicting the continuum on account of the large object-to-object variations in these regions. The typical  $1\sigma$  uncertainty of the PCA continuum fitting over the Ly $\alpha$  forest is less than 10%. Continuum fits and blue-side predictions are shown in Figure 1 along with the QSO spectra. We also verify that our dark gap statistics results do not significantly change if we use power-law continua (see Appendix C), which have a typical bias of  $\sim 10\%$  over the Ly $\alpha$  forest (Bosman et al. 2021b).

#### 3. Dark Gap Statistics

#### 3.1. Method

We define a dark gap to be a continuous spectral region in which all pixels binned to  $1h^{-1}$  Mpc have an observed normalized flux  $F = F_{\rm obs}/F_{\rm c} < 0.05$ , where  $F_{\rm obs}$  is the observed flux and  $F_{\rm c}$  is the continuum flux. The minimum length of a dark gap is  $1h^{-1}$  Mpc. We apply this definition when searching for dark gaps in both the real data and the mock spectra. The bin size and flux threshold were chosen to enable a uniform analysis over our large sample of spectra. A bin size of  $1h^{-1}$  Mpc (corresponding to a velocity interval of  $\Delta v \simeq 150 \, {\rm km \, s^{-1}}$  at z = 5.6) provides a convenient scale that preserves most of the structure of the Ly $\alpha$  forest. The choice of

Table 1 QSO Spectra Used in This Work

No.	QSO	z[Ref.] (3)	Source	Instrument	S/N
(1)	(2)	(3)	(4)	(5)	(6)
1	J2207-0416	5.529 <sup>b</sup>	archival (B19)	X-Shooter	42
2	J0108+0711	5.577 <sup>b</sup>	archival (B19)	X-Shooter	29
3	J1335-0328	5.693 <sup>b</sup>	archival (B19)	X-Shooter	30
4	SDSSJ0927+2001	5.7722°	archival (B19)	X-Shooter	76
5	SDSSJ1044-0125	5.7847°	other archival	ESI	71
6	PSOJ065+01	5.790 <sup>q</sup>	XQR-30	X-Shooter	47
7	PSOJ308-27	5.794 <sup>q</sup>	XQR-30	X-Shooter	58
8	SDSSJ0836+0054	5.810 <sup>g</sup>	other archival	ESI	152
9	PSOJ004+17	5.8165°	other archival	X-Shooter	21
10	SDSSJ0002+2550	5.820 <sup>b</sup>	archival (B19)	ESI	93
11	PSOJ242-12	5.834 <sup>q</sup>	XQR-30	X-Shooter	28
12	SDSSJ0840+5624	5.8441 <sup>n</sup>	archival (B19)	ESI	41
13	SDSSJ0005-0006	5.847 <sup>b</sup>	archival (B19)	ESI	24
14	PSOJ025-11	5.849 <sup>q</sup>	XQR-30	X-Shooter	53
15	PSOJ183-12	5.857 <sup>q</sup>	XQR-30	X-Shooter	66
16	SDSSJ1411+1217	5.904 <sup>g</sup>	archival (B19)	ESI	46
17	PSOJ108+08	5.950 <sup>q</sup>	XQR-30	X-Shooter	70
18	PSOJ056-16	5.9670 <sup>e</sup>	archival (B19)	X-Shooter	35
19	PSOJ029-29	5.981 <sup>q</sup>	XQR-30	X-Shooter	51
20	SDSSJ0818+1722	5.997 <sup>b</sup>	archival (B19)	X-Shooter	108
21	ULASJ0148+0600	5.998 <sup>b</sup>	archival (B19)	X-Shooter	126
22	PSOJ340-18	5.999 <sup>b</sup>	archival (B19)	X-Shooter	32
23	PSOJ007+04	6.0008 <sup>d</sup>	XOR-30	X-Shooter X-Shooter	53
24	SDSSJ2310+1855	6.0031°	XQR-30 XQR-30	X-Shooter	81
25	SDSSJ12310+1833 SDSSJ1137+3549	6.007 <sup>j</sup>	archival (B19)	ESI	28
26	ATLASJ029.9915-36.5658	6.021 <sup>b</sup>	XOR-30	X-Shooter	48
27	SDSSJ1306+0356	6.0330 <sup>k</sup>	archival (B19)	X-Shooter	71
28	J0408-5632	6.035 <sup>q</sup>	XOR-30	X-Shooter	71
29		6.0366 <sup>d</sup>	•		25
	ULASJ1207+0630		archival (B19)	X-Shooter	
30	SDSSJ2054-0005	6.0391°	archival (B19)	ESI	29
31	PSOJ158-14	6.0681 <sup>e</sup>	XQR-30	X-Shooter	59
32	SDSSJ0842+1218	6.0763 <sup>d</sup>	XQR-30	X-Shooter	71
33	SDSSJ1602+4228	6.079 <sup>j</sup>	archival (B19)	ESI	34
34	PSOJ239-07	6.1098 <sup>e</sup>	XQR-30	X-Shooter	65
35	CFHQSJ1509-1749	6.1225 <sup>d</sup>	archival (B19)	X-Shooter	54
36	SDSSJ2315-0023	6.124 <sup>b</sup>	archival (B19)	ESI	25
37	ULASJ1319+0950	6.1330°	archival (B19)	X-Shooter	86
38	SDSSJ1250+3130	6.137 <sup>j</sup>	new observation	ESI	53
39	VIKJ2318-3029	6.1458 <sup>d</sup>	archival (B19)	X-Shooter	21
40	PSOJ217-16	6.1498 <sup>d</sup>	XQR-30	X-Shooter	68
41	PSOJ217-07	6.165 <sup>q</sup>	XQR-30	X-Shooter	42
42	PSOJ359-06	6.1718 <sup>e</sup>	XQR-30	X-Shooter	67
43	PSOJ060+24	6.177 <sup>q</sup>	XQR-30	X-Shooter	53
44	PSOJ065-26	6.1877 <sup>d</sup>	XQR-30	X-Shooter	73
45	PSOJ308-21	6.2341 <sup>d</sup>	archival (B19)	X-Shooter	26
46	SDSSJ1030+0524	6.309 <sup>f</sup>	archival (B19)	X-Shooter	35
47	SDSSJ0100+2802	$6.3270^{1}$	archival (B19)	X-Shooter	212
48	ATLASJ025.6821-33.4627	6.3373 <sup>k</sup>	archival (B19)	X-Shooter	61
49	J1535+1943	6.381 <sup>q</sup>	XQR-30	X-Shooter	30
50	SDSSJ1148+5251	6.4189 <sup>h</sup>	archival (B19)	ESI	64
51	J1212+0505	6.4386 <sup>d</sup>	XQR-30	X-Shooter	41
52	J0439+1634	6.5188 <sup>p</sup>	new observation	X-Shooter	224
53	VDESJ0224-4711	6.5223 <sup>m</sup>	XQR-30	X-Shooter	29
54	PSOJ036+03	6.541 <sup>a</sup>	archival (B19)	X-Shooter	38
55	PSOJ323+12	6.5881 <sup>i</sup>	XQR-30	X-Shooter	30

Notes. Columns: (1) QSO index number; (2) QSO name; (3) QSO redshift with reference; (4) source of the spectrum used for dark gap statistics; (5) instrument used for dark gap statistics; (6) continuum signal-to-noise ratio per 30 km s<sup>-1</sup> near rest wavelength 1285 Å. Sources of the spectra are as follows. XQR-30: spectra from the XQR-30 program; new observation: spectra from new observations; archival (B19): archival spectra used and reduced in Becker et al. (2019); other archival: spectra from the public archives but not included in Becker et al. (2019). Redshift lines and their references are described below.

b [C II] 158  $\mu$ m: Bañados et al. (2015). Apparent start of the Ly $\alpha$  forest: Becker et al. (2019).

c CO: Carilli et al. (2007).

<sup>[</sup>C II] 158  $\mu$ m: Decarli et al. (2018).

e [C II] 158  $\mu$ m: Eilers et al. (2020).

Mg II: Jiang et al. (2007).

g Mg II: Kurk et al. (2007). h IG 20 150

<sup>[</sup>C II] 158  $\mu$ m: Maiolino et al. (2005).

<sup>[</sup>C II] 158  $\mu$ m: Mazzucchelli et al. (2017).

Mg II: Shen et al. (2019).

<sup>[</sup>C II] 158 µm: Venemans et al. (2020).

<sup>1 [</sup>C II] 158 µm: Wang et al. (2019). [C II] 158  $\mu$ m: Wang et al. (2021).

n CO: Wang et al. (2010).

CO: Wang et al. (2010).

o [C II] 158 μm: Wang et al. (2013).

p [C II] 158 μm: Yang et al. (2019).

q Apparent start of the Lyα forest: this work.

the flux threshold  $F_{\rm t}$  is mainly restricted by the quality of the data. Our choice of  $F_{\rm t}=0.05$  corresponds to nondetection of transmission lower than approximately twice the binned flux error  $(2\sigma)$  in the spectrum with the lowest S/N in our sample. Using such a threshold, all dark gaps longer than  $30h^{-1}$  Mpc have  $\tau_{\rm eff}>4$ . We have tested that using 0.1 or 0.025 for the flux threshold does not change our conclusions fundamentally when applying the same criteria to both the observed and mock spectra. Setting  $F_{\rm t}=0.1$  tends to yield dark gaps that are less opaque, while setting  $F_{\rm t}=0.025$  would decrease the number of usable QSO sightlines from 55 to 37.

In order to avoid the QSO proximity region, we identify dark gaps in the Ly $\alpha$  forest starting from 7 proper Mpc (pMpc) blueward from the QSO, which is close to the size of the largest proximity zones of bright OSOs at these redshifts (Eilers et al. 2017, 2020). On the blue end, we limit our search to greater than 1041 Å in the rest frame in order to avoid contamination from associated Ly $\beta$  or O VI absorption (e.g., Becker et al. 2015). For the purpose of comparing our results to simulations, we wish to avoid dark gaps that may be truncated by transmission peaks within the proximity zone. When quantifying the fraction of lines of sight that intersect gaps of length  $L \geqslant 30h^{-1}$  Mpc (Sections 3.4 and 3.5), the highest redshift at which we register an individual sightline that shows a long gap, if any, is therefore  $30h^{-1}$  Mpc blueward of our proximity zone cut, although the gap may include pixels that extend up to the proximity zone. Nevertheless, we still record the full lengths of gaps extending to this  $30h^{-1}$  Mpc "buffer zone" when searching for the longest possible dark gaps in both data and simulations. Dark gaps completely located in the OSO proximity zone and/or in this "buffer zone," however, are discarded. This ensures that the pixel at the red end of each sightline may intersect a long  $(L \ge 30h^{-1} \text{ Mpc})$  dark gap. <sup>18</sup> Finally, we limit our analysis to z < 6 because the mean transmitted flux at z > 6 is so low that most spectra show long dark gaps, making the dark gap statistics less informative.

We note that there is no perfect way to handle the proximity zone effect. It is difficult to precisely define and measure the proximity zone size for each QSO, which partly motivates our choice to use a fixed proximity zone cut. The proximity zone for the brightest QSOs in our sample (e.g., SDSS J0100+2802 and VDES J0224+4711) may be larger than our adopted cut of 7 pMpc. Fortunately, the use of an additional  $30h^{-1}$  Mpc buffer zone minimizes the potential effect of the larger proximity zone of these objects. In addition, because we limit our statistics over 5 < z < 6, proximity zone transmission at z > 6 toward some extremely bright QSOs does not impact our results. Still, one should treat dark gaps near the QSO proximity zone with caution.

Noisy residuals from skyline subtraction and telluric correction may divide an otherwise continuous region of depressed flux. To deal with this, when searching for dark gaps we mask out  $\pm 75~{\rm km~s^{-1}}$  intervals of the spectra centered at peaks in the flux error array, which typically correspond to skyline residuals. The exception to this is that we do not mask

out any pixels with  $F > 3\sigma_F$ . For consistency, we apply the same masking procedure to the mock spectra. <sup>19</sup> In Appendix B, we use the mock spectra to show that such masking only produces a minor change in the results. We also test that the impact of masking telluric correction residuals near 7600-7650 Å is neglectable.

As for contamination from damped Ly $\alpha$  systems (DLAs) or other metal-enriched absorbers, we made no correction for their effect on dark gap detection following, e.g., Fan et al. (2006). Even strong DLAs can hardly, on their own, produce dark gaps as long as 30  $h^{-1}$  Mpc, which are the primary focus of this work. Nevertheless, in the results we label dark gaps with intervening metal systems for reference based on the systems identified by Chen et al. (2017) and Becker et al. (2019), as well as our own inspections. We visually searched all  $L \ge 30h^{-1}$  Mpc dark gaps for metal absorbers not listed in the literature. The systems were identified via the coincidence of multiple metal lines in redshift. The metal lines we used include C II  $\lambda$ 1334, C IV  $\lambda\lambda$ 1548, 1550, O I  $\lambda$ 1302, Mg II  $\lambda\lambda 2797$ , 2803, Al II  $\lambda 1670$ , Si II  $\lambda 1527$ , and Si IV  $\lambda\lambda 1394$ , 1403. A detection required these metal lines (if available) to have significant absorption features and self-consistent velocity profiles at the same redshift. We have a good wavelength coverage for most metal lines mentioned above in QSO spectra taken with X-Shooter. Even for these objects, however, we caution that the list of metal absorbers may be still incomplete. A full list of metal absorbers in the XQR-30 spectra will be presented by R. Davies et al. (2021, in preparation). We also note that the simulations we used do not include DLAs or other metal-enriched absorbers.

# 3.2. Notable Dark Gaps

Long dark gaps play an important role in characterizing the IGM in the later stages of reionization. Among 50 dark gaps with  $L \ge 30h^{-1}$  Mpc detected in our sample, Figure 2 displays some notable examples. They either extend down to or below  $z \sim 5.5$ , are extremely long  $(L > 80h^{-1}$  Mpc), or both.

Two long dark gaps entirely at z < 5.5 are identified toward PSO J183-12 and PSOJ340-18. They span  $z_{\rm gap} = 5.36 - 5.47$  and  $z_{\rm gap} = 5.31 - 5.42$ , corresponding to lengths of  $L = 37h^{-1}$  Mpc and  $L = 34h^{-1}$  Mpc, respectively. Most spikes and sharp dips with negative flux in the unbinned spectra inside the two gaps are skyline subtraction residuals, as indicated by the peaks in the flux error array. Both dark gaps are highly opaque, with  $\tau_{\rm eff} > 6$ . The spectra of both QSOs have a good coverage of redshifted common metal lines. We searched their X-Shooter VIS and NIR spectra and found no metal absorption within the redshift ranges of the dark gaps. In addition, a  $30h^{-1}$  Mpc dark gap extending just above z = 5.5 is identified toward SDSS J1250+3130. Most of the spikes inside this gap are also probably due to sky lines as indicated by peaks in the flux error array.

The fourth through sixth rows in Figure 2 display three examples of long dark gaps extending down to  $z \sim 5.5$ . The long gap extending to z = 5.46 with a length of  $L = 68h^{-1}$  Mpc toward PSOJ025-11 is one of the longest troughs below redshift six discovered in this work. The only weak

 $<sup>\</sup>overline{}^{17}$  Throughout this paper,  $au_{\rm eff}$  of a dark gap is calculated based on flux averaged along the full length of the gap rather than over windows of a fixed length. Most low  $au_{\rm eff}$  values for short dark gaps are caused by skyline subtraction or telluric correction residuals.

subtraction or telluric correction residuals. 

18 If we do not introduce this "buffer zone," there is a possibility that the  $F_{30}$  (Section 3.4) is underestimated near the red end of a sightline, since there can exist otherwise  $> 30h^{-1}$  Mpc gaps that are truncated by the edge or peaks in the proximity zone.

 $<sup>\</sup>overline{^{19}}$  Since we add noise to the mock spectra pixel-wise according to the noise array of each observed spectrum with a Gaussian distribution, the skyline residuals in the mock spectra are not actually modeled. However, masking  $\pm 75~{\rm km~s^{-1}}$  intervals makes the profile of sky subtraction residuals unimportant.

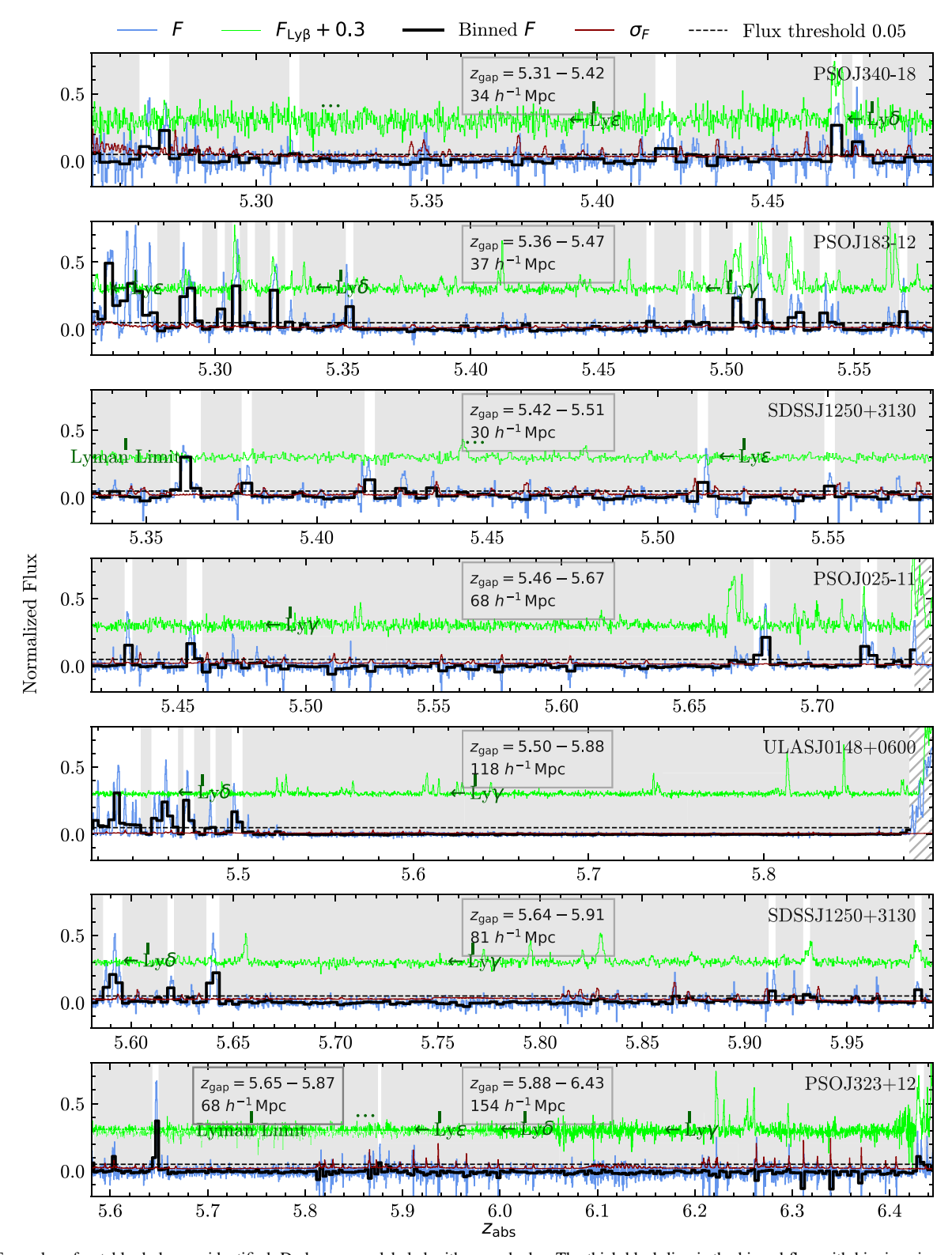


Figure 2. Examples of notable dark gaps identified. Dark gaps are labeled with gray shades. The thick black line is the binned flux with binning size of  $1h^{-1}$  Mpc. Dashed black horizontal line sets the flux threshold of 0.05. Unbinned flux and flux uncertainty are represented by thin blue and dark red lines, respectively. The text boxes display the redshift span and length of each long dark gap ( $L \ge 30h^{-1}$  Mpc). Regions redward the proximity zone cut are labeled with hatches and are excluded from the statistics. For reference, the green line, offset by 0.3 in flux, is shifted in wavelength to show the Ly $\beta$  and higher-order Lyman forest at the same redshifts. Vertical ticks label the starting points of higher-order Lyman forests.

transmission peaks in the unbinned flux array that seem to be real are the ones at  $z_{\rm abs} \simeq 5.47$ , 5.48, and 5.67. Overall, however, it is extremely dark, with  $\tau_{\rm eff} \geqslant 6.4$ . We also

reproduce the detection of the long trough discovered toward ULAS J0148+0600 by Becker et al. (2015), which extends down to z = 5.5 with a total length  $L > 110h^{-1}$  Mpc. Due to the

**Table 2**Properties of Dark Gaps

Index (1)	QSO (2)	Z <sub>blue</sub> (3)	z <sub>red</sub> (4)	$L(h^{-1} \operatorname{Mpc}) $ (5)	$ au_{ m eff} \  ag{6}$	z <sub>absorber</sub> (7)
26	ULASJ1319+0950	5.876	6.012 <sup>b</sup>	<i>≥</i> 40	≥ 6.674	
157	SDSSJ0100+2802	5.883	5.988	31	$7.874 \pm 0.339$	5.945, 5.940
240	PSOJ108+08	5.661	5.836 <sup>b</sup>	<i></i> ≥54	$6.062 \pm 0.145$	
281	PSOJ183-12	5.332	5.350	6	$4.193 \pm 0.133$	
292	PSOJ183-12	5.690	5.702	4 <sup>c</sup>	$3.951 \pm 0.082$	
294	SDSSJ1602+4228	5.065	5.071	2	$3.580 \pm 0.251$	
350	ATLASJ025.6821-33.4627	5.285 <sup>a</sup>	5.356	24	$5.680 \pm 0.226$	
817	SDSSJ1148+5251	5.853	6.285 <sup>b</sup>	≥124	≥7.558	6.258, 6.011, 6.131
959	SDSSJ1137+3549	5.683	5.686	1	≥ 3.569	

Notes. Columns: (1) index of the dark gap; (2) QSO name; (3) redshift at the blue end of the gap; (4) redshift at the red end of the gap; (5) dark gap length; (6) effective opacity of the dark gap based on the flux and flux error in the original binning; (7) redshift(s) of known metal absorber(s) in the dark gap, if any.

(This table is available in its entirety in machine-readable form.)

use of a different definition of dark gap compared to Becker et al. (2015), the trough detected in this work includes an additional small transmission peak that appears in the unbinned spectrum near the blue end. This yields a slightly larger L but a comparable  $\tau_{\rm eff}$  value. We also find a gap of  $L = 81h^{-1}{\rm Mpc}$ extending down to z = 5.64 toward SDSS J1250+3130. Spikes within the trough are skyline subtraction residuals, as shown by peaks in the error array. We do not see any strong metal absorbers that would indicate dense absorption systems such as DLAs or Lyman limit systems (LLSs), in any of these gaps. Finally, we find dark gaps longer than  $110h^{-1}$  Mpc toward several QSOs with the highest redshifts in our sample. This is not surprising because the IGM is more neutral at higher redshifts and therefore more likely to produce large Ly $\alpha$ opaque regions. For example, Barnett et al. (2017) identified a  $240h^{-1}$  Mpc gap at z > 6.1 toward the z = 7.1 QSO ULAS J1120+0641. Here we display a remarkably long dark gap toward PSO J323+12. It covers  $z_{\text{gap}} = 5.88-6.43$  and has a length of  $154h^{-1}$  Mpc, as shown in the bottom row of Figure 2.

For reference, we overplot in green the regions of spectra corresponding to  $\text{Ly}\beta$  for the  $\text{Ly}\alpha$  shown in Figure 2. In many cases, the  $\text{Ly}\beta$  forest also includes higher order Lyman series absorption, as indicated in the figure. Although dark gaps are highly opaque to  $\text{Ly}\alpha$ , there are often narrow transmission peaks corresponding to  $\text{Ly}\beta$ . These peaks demonstrate that the dark gaps in  $\text{Ly}\alpha$  typically cannot arise from continuous regions of neutral gas, which would be highly opaque to all Lyman series lines. Broken regions of neutral gas may still be present, however, with the  $\text{Ly}\beta$  transmission corresponding to gaps between neutral sections (e.g., Keating et al. 2020b; Nasir & D'Aloisio 2020).

# 3.3. Overview of Dark Gaps

In total, we detected 1329 dark gaps from the sample, of which 50 have a length of  $L \ge 30h^{-1}$  Mpc. Properties of all dark gaps detected are summarized in Table 2. Details on dark gap detection for each QSO sightline are shown in Figure 1.

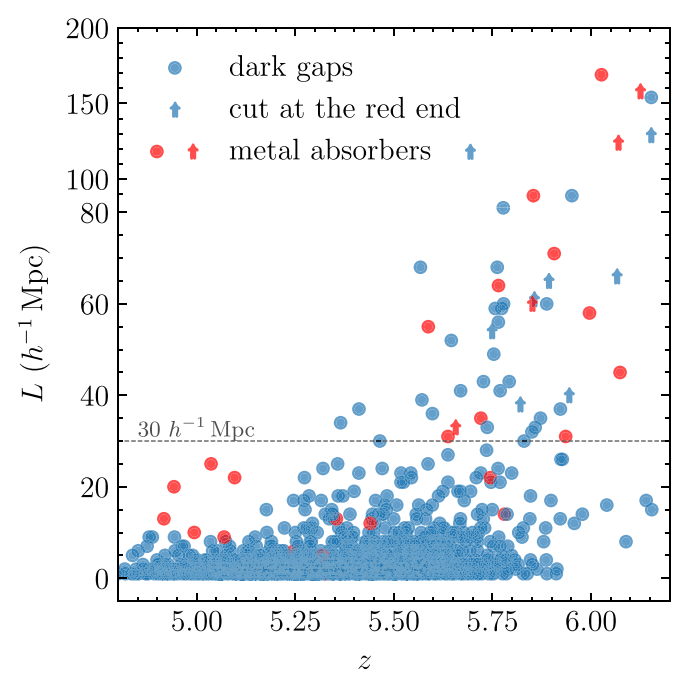


**Figure 3.** Gap length vs. central redshift for dark gaps detected from our sample. Dark gaps located completely in the "buffer zone" are excluded from this plot. Arrows indicate dark gaps whose red edge lies within 7 pMpc from the QSO and are therefore potentially truncated by the proximity effect; lower limits on the length are therefore given for these gaps. Red symbols indicate dark gaps with one or more metal absorbers.

As an overview, Figure 3 plots all dark gaps identified in this work according to their central redshift and length. Dark gaps with associated metal absorbers are labeled in red. This figure has excluded dark gaps that are completely inside the 7 pMpc proximity zone and/or inside the  $30h^{-1}$  Mpc "buffer zone" beyond the proximity zone. Not surprisingly, as redshift increases, there are more long dark gaps and a larger scatter in dark gap length. The lowest-redshift gaps with  $L \ge 30h^{-1}$  Mpc appear around z = 5.3.

Figure 4 displays the Ly $\alpha$  forest coverage and all dark gaps identified for every line of sight in our sample. At  $z \lesssim 5.2$ , most QSO sightlines are highly transmissive; a few gaps with

Dark gap starting at the blue edge of the Ly $\alpha$  forest.

b Dark gap ending at the red edge of the Ly $\alpha$  forest.

<sup>&</sup>lt;sup>c</sup> Dark gap located completely inside the buffer zone.

 $<sup>\</sup>overline{^{20}}$  We use a power law to fit the continuum for regions blueward of the Ly $\alpha$  forest because our PCA implementation does not cover these wavelengths; however, this should not significantly affect the qualitative results for the higher-order Lyman series transmission shown in Figure 2.

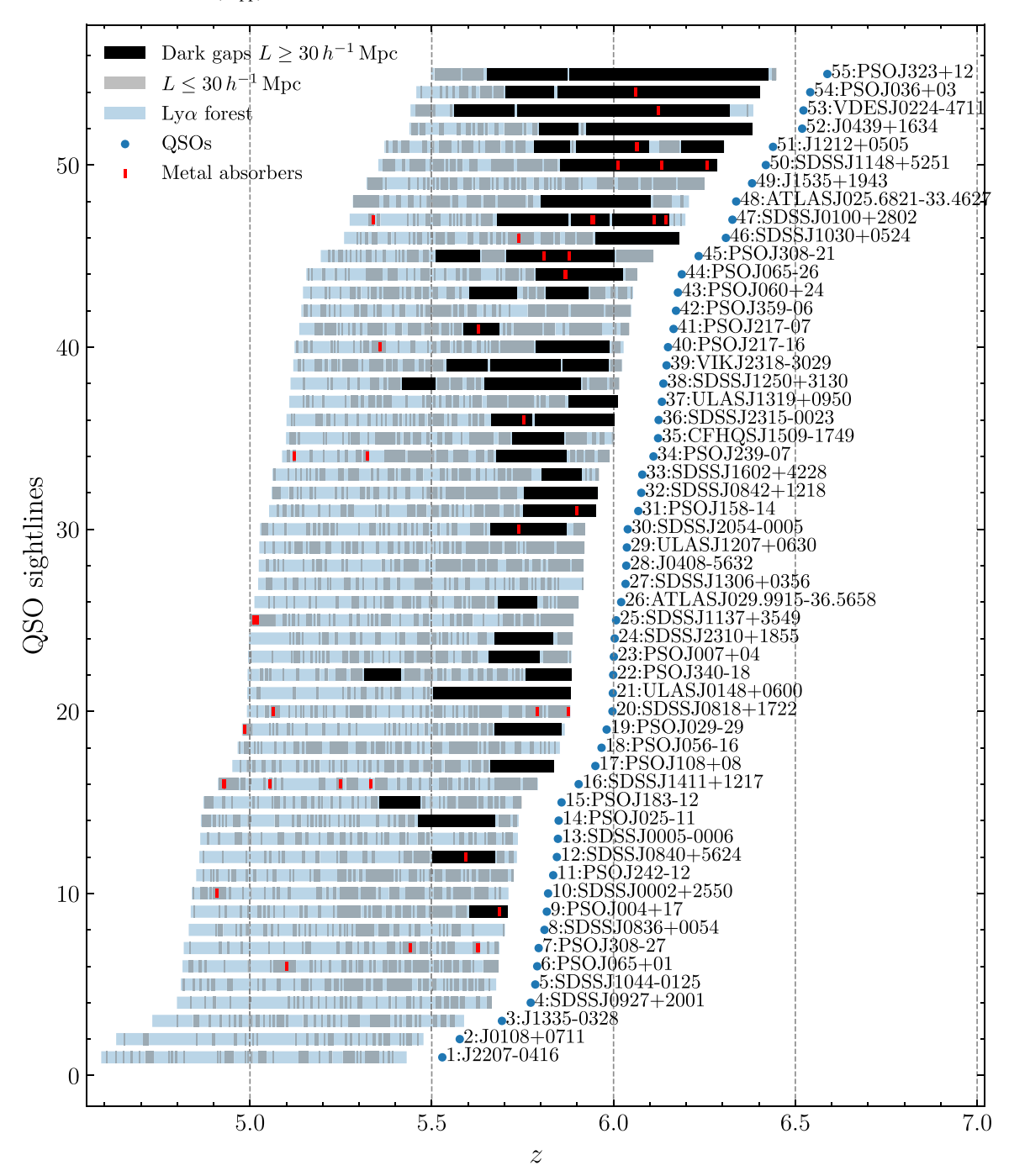
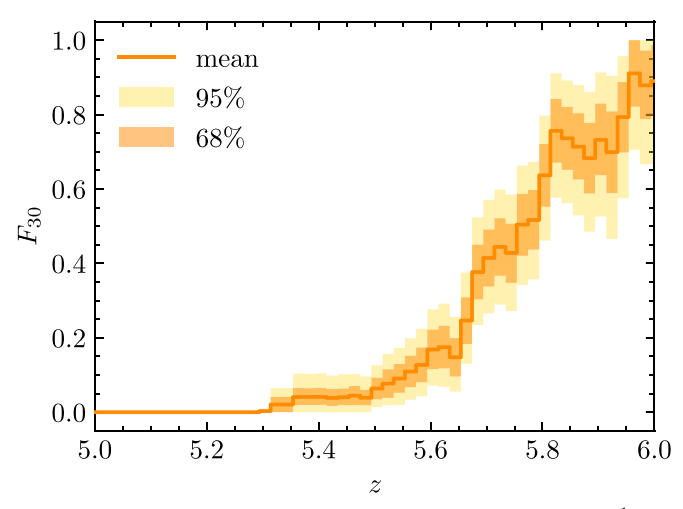


Figure 4. Overview of dark gaps identified in the Ly $\alpha$  forest of 55 QSO sightlines. Black bars and gray shaded regions represent dark gaps longer and shorter than  $30h^{-1}$  Mpc, respectively. Red short lines denote known associated metal absorbers intervening dark gaps. Light blue shaded regions indicate the redshift coverage of the Ly $\alpha$  forest. Redshifts of QSOs are marked with blue dots. The Ly $\alpha$  forest is truncated at 7 pMpc from the QSO. The Ly $\alpha$  forest shown in this figure *includes* the  $30h^{-1}$  Mpc buffer zone on the red end, which is excluded from the statistical analysis of dark gaps. See Section 3.1 for details.

 $L \sim 10-20\,h^{-1}$  Mpc appear but these tend to contain metal absorbers and are likely to be DLAs. Dark gaps longer than  $30h^{-1}$  Mpc appear in the sightlines of PSO J340-18 and PSO J183-12 at  $z \simeq 5.3$  and 5.4, respectively. The frequency of long dark gaps increases with redshift, such that most lines of sight at  $z \simeq 5.8$  show gaps longer than  $30h^{-1}$  Mpc in the Ly $\alpha$  forest. Interestingly, the J1535+1943 sightline is relatively transmissive at  $z \sim 6$  compared to others at the same redshift. Although J1535 has a reddened spectrum, the continuum reconstruction is acceptable and most of the transmission peaks in the Ly $\alpha$  forest appear to be real.

### 3.4. Fraction of QSO Spectra Exhibiting Long Dark Gaps

We introduce the fraction of QSO spectra exhibiting long  $(L \ge 30h^{-1} \text{ Mpc})$  gaps as a function of redshift,  $F_{30}(z)$ , as a new Ly $\alpha$  forest statistic. As mentioned in Section 3.1, in order to deal with the finite length of the spectra for this statistic we cut off each QSO sightline at the blue edge of the  $30h^{-1} \text{ Mpc}$  buffer zone.  $F_{30}$  quantifies how common the large Ly $\alpha$ -opaque regions are and how they evolve with redshift. We choose  $30h^{-1} \text{ Mpc}$  because we found that this length most effectively distinguishes between the models described in Section 4, especially between the homogeneous-UVB and other



**Figure 5.** Measured fraction of QSO spectra exhibiting long ( $L \ge 30h^{-1}$  Mpc) dark gaps as a function of redshift. We use bootstrap resampling to calculate the mean, 68% limit, and 95% limit of  $F_{30}$  averaged over  $\Delta z = 0.02$  bins, presented with the solid orange line, dark-shaded region, and light-shaded region, respectively.

(The data used to create this figure are available.)

models. The comparison of the dark gap length distribution, P(L), predicted by different models in Section 4.5 also implies that dark gaps with  $L \ge 30h^{-1}$  Mpc are potentially good probes for H I if the late reionization scenario is indeed preferred. We note that we include all long dark gaps regardless of the presence of associated metal absorbers since the dense absorption systems alone are not likely to create troughs longer than  $30h^{-1}$  Mpc.

Figure 5 displays the evolution of  $F_{30}$  with redshift measured from the QSO spectra. The result is averaged over  $\Delta z = 0.02$  bins. The mean, 68% limits, and 95% limits of  $F_{30}$  are calculated based on 10,000 bootstrap resamplings of the whole sample. In each realization, we randomly select 55 QSO spectra, with replacement, and add up the number of sightlines showing  $L \ge 30h^{-1}$  Mpc dark gaps at a given redshift. The total is then normalized by the number of QSO sightlines at each redshift, which yields  $F_{30}(z)$  for this realization.  $F_{30}$  starts to be nonzero from  $z \simeq 5.3$  and increases strongly with redshift. At z = 6,  $\sim 90\%$  of sightlines present long gaps.

We noted above that a deep spectrum of SDSS J1250+3130 was obtained based on preliminary indications from shallower data of a long gap in its spectrum. This is the only QSO in the sample for which the selection is related to the foreknowledge of dark gaps. We include J1250 for completeness, but note that excluding this line of sight from our sample would only decrease (increase)  $F_{30}$  by  $\lesssim 0.02$  (0.05) over 5.50 < z < 5.90 (5.90 < z < 5.93).

Finally, we test whether metal absorbers could be linking adjacent dark gaps in a way that would impact our  $F_{30}$  statistic. For this, we calculate a "pessimistic"  $F_{30}$  by dividing dark gaps at the redshifts of DLAs and other metal systems (Appendix D). The resulting change in  $F_{30}$  is minor, with a maximum decrease of  $\sim 0.1$  at  $z \sim 5.8$ . The differences between the observations and model predictions (Section 5.1; Figure D1) can still be well distinguished. We therefore conclude that this potential impact of metal absorbers on  $F_{30}$  is not significant.

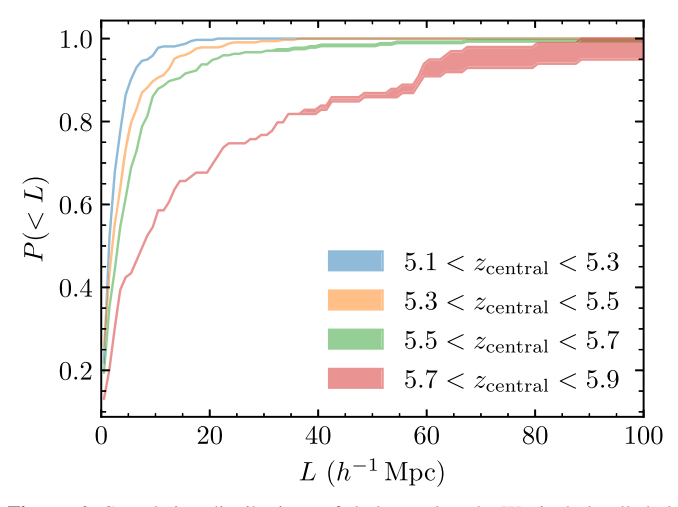


**Figure 6.** Cumulative distributions of dark gap length. We include all dark gaps regardless of the presence of associated metal absorbers. The upper and lower bounds of the shaded regions correspond to the most pessimistic and optimistic cases for P(< L). See text for details.

#### 3.5. Distribution of Dark Gap Length

In addition to  $F_{30}$ , we investigate the cumulative distribution function (CDF) of gap length, P(<L). Figure 6 plots P(<L) in redshift bins of  $\Delta z = 0.2$ . Dark gaps are assigned to a bin based on the central redshift of the gap, and we do not truncate gaps extending beyond the edges of the redshift windows. We treat the dark gaps truncated by the 7 pMpc proximity zone cut by plotting the most pessimistic and optimistic bounds on P(<L). The pessimistic bound is calculated by considering the lengths of dark gaps are as measured. The optimistic bound, however, is given by assuming the lengths of truncated dark gaps are infinite, which indicates the most extreme dark gap length possible in the absence of the QSO. In the latter case, we still use the measured central redshift of each dark gap to assign it to a redshift bin.

Figure 6 demonstrates that longer dark gaps become more common toward higher redshifts. This is consistent with the result of  $F_{30}$ . Moreover, similar to the rapid redshift evolution in  $F_{30}$  near  $z \simeq 5.7$ , P(< L) shows a large change between 5.5 < z < 5.7 and 5.7 < z < 5.9.

To test the effects of metal absorbers on P(< L), we calculate the distribution by excluding dark gaps with known associated metal absorbers. We find the difference is minor. The maximum increment on the most pessimistic P(< L) over 5.7 < z < 5.9 is less than 0.03, and the difference is less than 0.005 over the other redshift bins.

#### 4. Models and Simulations for Comparison

We compare our measurements to predictions from hydrodynamical simulations that span a range of reionization histories and UV backgrounds. Here we briefly describe the simulations. The key information is summarized in Table 3, with the redshift evolution of the volume-weighted neutral hydrogen fraction  $\langle x_{\rm HI} \rangle$  for each simulation plotted in Figure 7.

# 4.1. Homogeneous UV Background

We first include a baseline model, wherein reionization is fully completed at z > 6 and the UVB is spatially uniform. For this, we use a run from the Sherwood simulation suite, which successfully reproduces multiple characteristics of the observed

Table 3
Models Used in This Work

Model (1)	Reionization (2)	z <sub>95</sub> (3)	z <sub>50</sub> (4)
homogeneous-UVB		15	
K20-low- $ au_{ ext{CMB}}$	late	5.6	6.7
K20-low- $ au_{ ext{CMB}}$ -hot	late	5.6	6.7
K20-high- $ au_{ ext{CMB}}$	late	5.9	8.4
ND20-late-longmfp	late	5.3	7.0
ND20-late-shortmfp	late	5.4	7.5
ND20-early-shortmfp	early	6.6	8.7

**Note.** Columns: (1) name of the model; (2) qualitative description of the reionization model; (3) redshift at which the volume-filling factor of ionized gas reaches 95%; (4) redshift at which the volume-filling factor of ionized gas reaches 50%, We use K20 for models from Keating et al. (2020a) and ND20 for models from Nasir & D'Aloisio (2020). See Sections 4.2 and 4.3 for details.

Ly $\alpha$  forest over 2.5 < z < 5 (Bolton et al. 2017). The Sherwood suite uses a homogeneous Haardt & Madau (2012) UV background. Reionization occurs instantaneously at z = 15, allowing the IGM to fully relax hydrodynamically by z = 6. The simulations were run with the parallel smoothed particle hydrodynamics code P-GADGET-3, which is an updated and extended version of GADGET-2 (Springel 2005). We use the simulation with  $2 \times 2048^3$  particles and box size of  $(160 \ h^{-1} \ \text{Mpc})^3$  to build mock spectra for the homogeneous-UVB model, as described in Section 4.4.

#### 4.2. Late Reionization

We use two sets of models wherein reionization continues significantly below redshift six. In these models, long dark gaps in Ly $\alpha$  transmission at z < 6 arise from a combination of neutral islands and regions of suppressed UVB, which are often adjacent to one another.

The first late reionization models are from Keating et al. (2020a). They include three models with different ionization and/or thermal histories. We denote the fiducial model as  $K20-low-\tau_{CMB}$ , wherein the volume-filling fraction of ionized gas reaches 95% at z = 5.6 and 99.9% at z = 5.2. the K20-low- $\tau_{\rm CMB}$ -hot runs, K20-high- $\tau_{\text{CMB}}$  models, are also included. Briefly, the K20-low- $\tau_{\text{CMB}}$ -hot model uses a higher temperature for the input blackbody ionizing spectrum, namely T = 40,000 Kinstead of  $T = 30,000 \,\mathrm{K}$  as used in the K20-low- $\tau_{\mathrm{CMB}}$ model. They have a volume-weighted mean temperature at the mean density at z = 6 of  $T_0 \simeq 10,000$  K and 7000 K, respectively. The K20-high- $\tau_{\rm CMB}$  model shares a similar IGM thermal history with the K20-low- $\tau_{\rm CMB}$  model, but it has an earlier reionization midpoint of  $z_{\text{mid}} = 8.4$ .

The K20 simulations are modified versions of the late reionization model published in Kulkarni et al. (2019a). The model was modified, such that (i) the IGM temperature evolution is in better agreement with recent observations (Boera et al. 2019; Walther et al. 2019; Gaikwad et al. 2021), and (ii) the mean Ly $\alpha$  transmission is in better agreement with data at z < 4.7 (Becker et al. 2015). The ionization state of the IGM is modeled using the radiative transfer code ATON (Aubert & Teyssier 2008, 2010) that postprocesses underlying hydrodynamic simulations performed with P-GADGET-3. The simulations use the identical initial condition and box size of

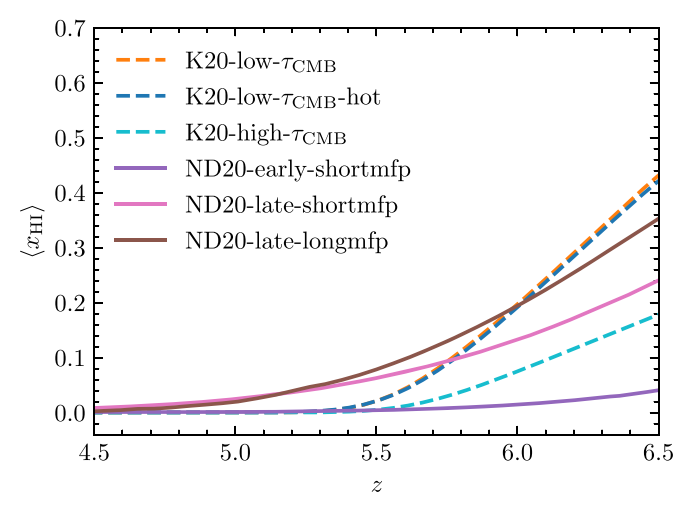


**Figure 7.** Redshift evolution of the volume-weighted average neutral hydrogen fraction of reionization models used in this work. See Table 3 for the key information of these models and details in Section 4.

the Sherwood simulation suite. The radiative transfer, however, leads to an extended and self-consistent reionization history. This produces scatter in the Ly $\alpha$   $\tau_{\rm eff}$ . The simulations also contain fluctuations in temperature and photoionization rates. A light cone from the radiative transfer simulation was extracted on the fly. Using sightlines through this light cone, Keating et al. (2020a) computed the optical depths continuously spanning  $4.0 \lesssim z \lesssim 7.5$  for each model, which allows us to avoid having to do any interpolation.

The second set of late reionization models is from Nasir & D'Aloisio (2020). In these models, the volume-filling factor of ionized gas reaches 95% at z=5.3–5.4. As in the Keating et al. (2020a) models, fluctuations in both the UVB and temperature are present. The UVB fluctuations are driven by a short and spatially variable mean free path, similar to the model in Davies & Furlanetto (2016). In the two Nasir & D'Aloisio (2020) models, which we denote as ND20-late-longmfp and ND20-late-shortmfp, the volume-weighted average mean free path for 912 Å photons at z=5.6 is  $\langle \lambda_{\rm mfp}^{912} \rangle = 30~h^{-1}\,{\rm Mpc}$  and  $10h^{-1}\,{\rm Mpc}$ , respectively. As a result of the shorter mean free path, ND20-late-shortmfp contains stronger fluctuations in the UVB. The shorter  $\langle \lambda_{\rm mfp}^{912} \rangle$  is also more consistent with the recent mean free path measurement of Becker et al. (2021).

The Nasir & D'Aloisio (2020) simulations use a modified version of the Eulerian hydrodynamics code from Trac & Pen (2004). They use  $2 \times 2048^3$  gas and dark matter resolution elements and a box size of  $L = 200h^{-1}$  Mpc. To model the effects of reionization on the forest, they postprocess the hydrodynamics simulations using seminumeric methods. Optical depth skewers are available at z = 5.6, 5.8, and 6.0, and neutral fraction information is available at z = 5.6 and 5.8. A sample of 4000 lines of sight were extracted at each redshift, with each optical depth skewer having a length of  $500h^{-1}$  Mpc by making use of the periodic boundary conditions (F. Nasir, private communication).

# 4.3. Early Reionization with a Fluctuating UVB

Finally, we include a model from Nasir & D'Aloisio (2020) wherein the volume-filling factor of ionized gas reaches  $\sim 98\%$  by z = 6, but the UVB retains large spatial fluctuations to

somewhat lower redshifts. It has  $\langle \lambda_{\rm mfp}^{912} \rangle = 10~h^{-1}$  Mpc as in the ND20-late-shortmfp model. We refer to this model as ND20-early-shortmfp. It is essentially a modified version of the fluctuating UVB model proposed by Davies & Furlanetto (2016) with temperature fluctuations included. Compared to the ND20-late-shortmfp model mentioned previously, the ND20-early-shortmfp model has a similarly broad UVB distribution but a much earlier end of reionization. In this model, long dark gaps at z < 6 primarily correspond to regions with a low UVB. Since the IGM is not technically fully ionized in this model until down to  $z \simeq 5$ , however, a small fraction of dark gaps may still contain some neutral hydrogen.

#### 4.4. Construction of Mock Spectra

In order to directly compare the observations to the models we construct mock spectra from the simulations with properties similar to the real data. We first describe how we create mock spectra for the homogeneous-UVB model.

The snapshots for the homogeneous-UVB model are available on every  $\Delta z = 0.1$  interval over  $3.9 \le z \le 8.9$ . To be consistent with the simulations from Nasir & D'Aloisio (2020) we only use snapshots from every  $\Delta z = 0.2$ , and the same snapshots are used for every sightline. We have verified, however, that using snapshots spaced every  $\Delta z = 0.1$  would not significantly impact our results. Each snapshot was used to extract 5000  $160h^{-1}$  Mpc skewers along which the native Ly $\alpha$ optical depths have been calculated (Bolton et al. 2017). For a mock spectrum centered at redshift  $z_0$  we combine skewers from redshifts  $z_0 - 0.2$ ,  $z_0$ , and  $z_0 + 0.2^{22}$  after shifting the periodic lines of sight by random amounts. The resulting mock spectra are still  $160h^{-1}$  Mpc in length but contain information about the redshift evolution of the Ly $\alpha$ -opaque regions. We fit the  $\tau_{\rm eff}$  evolution over  $5 \leqslant z \leqslant 6$  from Bosman et al. (2018) with a power law of  $\tau_{\rm eff} \propto (1+z)^{12.34}$  and renormalize the optical depths of the mock spectra such that their average Ly $\alpha$ transmission matches this evolution. We have also checked that the mean transmission measured directly from our observed sample is within the  $1\sigma$  uncertainties of the measurement in Bosman et al. (2018). We create 5000 mock spectra matching each of our 55 lines of sight. For each QSO, we bin the mock spectra using exactly the same wavelength arrayas the observed spectrum. We then add Gaussian noise to the mock spectra based onthe correspondingflux error array.

Because each optical depth skewer from the Nasir & D'Aloisio (2020) models has a length of  $500h^{-1}$  Mpc, we first clip them to  $160h^{-1}$  Mpc and then follow a similar procedure to build the mock spectra set at  $z_0$ =5.8 as described above, including rescaling the effective optical depth. In order to cover the full redshift range of the simulation outputs, we extend the mock spectra down to z = 5.6 and up to z = 6.0 by making use of the unclipped skewers to create mock spectra sets centered at  $z_0$ =5.6 and 6.0. However, because the spatial structure of the IGM is only recovered over  $5.6 \le z \le 6.0$ , we restrict our dark gap analysis to this redshift range. As for K20 models, Keating et al. (2020a) ran many radiative transfer simulations until they

converged on a reionization history that self-consistently reproduces the mean flux of the  $Ly\alpha$  forest as measured by Bosman et al. (2018). We therefore only needed to rebin the skewers and add noise in order to match them to each individual observed QSO spectrum. We note that continuum errors are not considered for the mock spectra. This is because the continuum errors for the observed spectra are estimated to be small ( $\lesssim$ 10%; Section 2.2), and partly because we are primarily concerned with very low flux levels, which are less affected in an absolute sense by continuum uncertainties.

In Figure 8, we display mock spectra randomly selected from all the models with S/N chosen to match the the Ly $\alpha$  forest of ULAS J0148+0600 as examples. The homogeneous-UVB model exhibits more small transmission peaks than the other models, as expected because the IGM is fully ionized by a uniform UVB. The other models tend to show longer dark gaps interspersed with regions of high transmission.

#### 4.5. Neutral Islands and Dark Gaps

Here we examine the connection between dark gaps and regions of neutral hydrogen. For this we calculate the dark gap length distribution P(L) predicted by models. We use the method described in Section 3.1 to find dark gaps in mock spectra generated in Section 4.4, but with no noise added, and identify gaps that contain regions of neutral hydrogen. The frequency of dark gaps with length L for each model in each redshift bin is calculated based on 10,000 realizations and normalized by the total count of dark gaps in each redshift bin, with P(L) averaged over bins of  $\Delta L = 5h^{-1}$  Mpc. We consider a dark gap to contain neutral hydrogen if any pixels inside this gap have  $x_{\rm HI} > 0.9$ . Over each redshift bin, dark gaps extending beyond the boundaries of the  $\Delta z = 0.2$  window are truncated at the edge. We do so to avoid artifacts in P(L) caused by the finite length of the mock spectra.

As shown in Figure 9, P(L) varies significantly between models. First, no dark gaps with neutral pixels are found in the homogeneous-UVB model because the IGM is fully ionized. In the ND20-early-shortmfp model, the IGM is 98%ionized by z = 6, and therefore only a small fraction of dark gaps contain neutral islands. Dark gaps with no neutral islands also dominate in the K20-high-  $\tau_{\rm CMB}$  model that has an extended reionization history. The situation is very different in the rapid late reionization scenarios, however. Dark gaps with neutral islands become dominant for  $L \ge 15-20 \ h^{-1} \,\mathrm{Mpc}$  in both ND20-late models. Similarly, in the K20-low $au_{\rm CMB}$  (-hot) model, dark gaps with neutral islands start to be the majority for  $L \gtrsim 25-30 \ h^{-1}$  Mpc at z > 5.4. Long dark gaps with  $L \gtrsim 30h^{-1}$  Mpc are therefore of potentially high interest in terms of identifying regions of the IGM that may contain neutral gas. This paper is therefore largely focused on these long gaps.

We further investigate the correlation between neutral islands coverage and dark gap length in the  $K20-10w-\tau_{CMB}$  model at different redshift, as shown in Figure 10. The histogram is calculated based on 10,000 realizations, and we include all dark gaps regardless of whether they contain neutral pixels. The neutral islands coverage shown here is the sum of the line-of-sight length of neutral pixels inside a dark gap. The mean neutral islands coverage is proportional to the dark gap length, meaning that long dark gaps may contain more neutral gas. Nevertheless, the neutral islands coverage is, on average, significantly less than the dark gap length. This suggests that

 $<sup>\</sup>overline{^{21}}$  The volume-filling factor of ionized gas no longer increases significantly at z < 6. Although it has not reached 99% strictly by z = 6, we still consider this model as an early reionization model.

<sup>&</sup>lt;sup>22</sup> We cut the skewers into three pieces and then stitch the corresponding pieces with those from the adjacent redshifts. Only a portion of a  $160h^{-1}$  Mpc skewer from a given snapshot is therefore used for a mock spectrum centered at  $z_0$ .

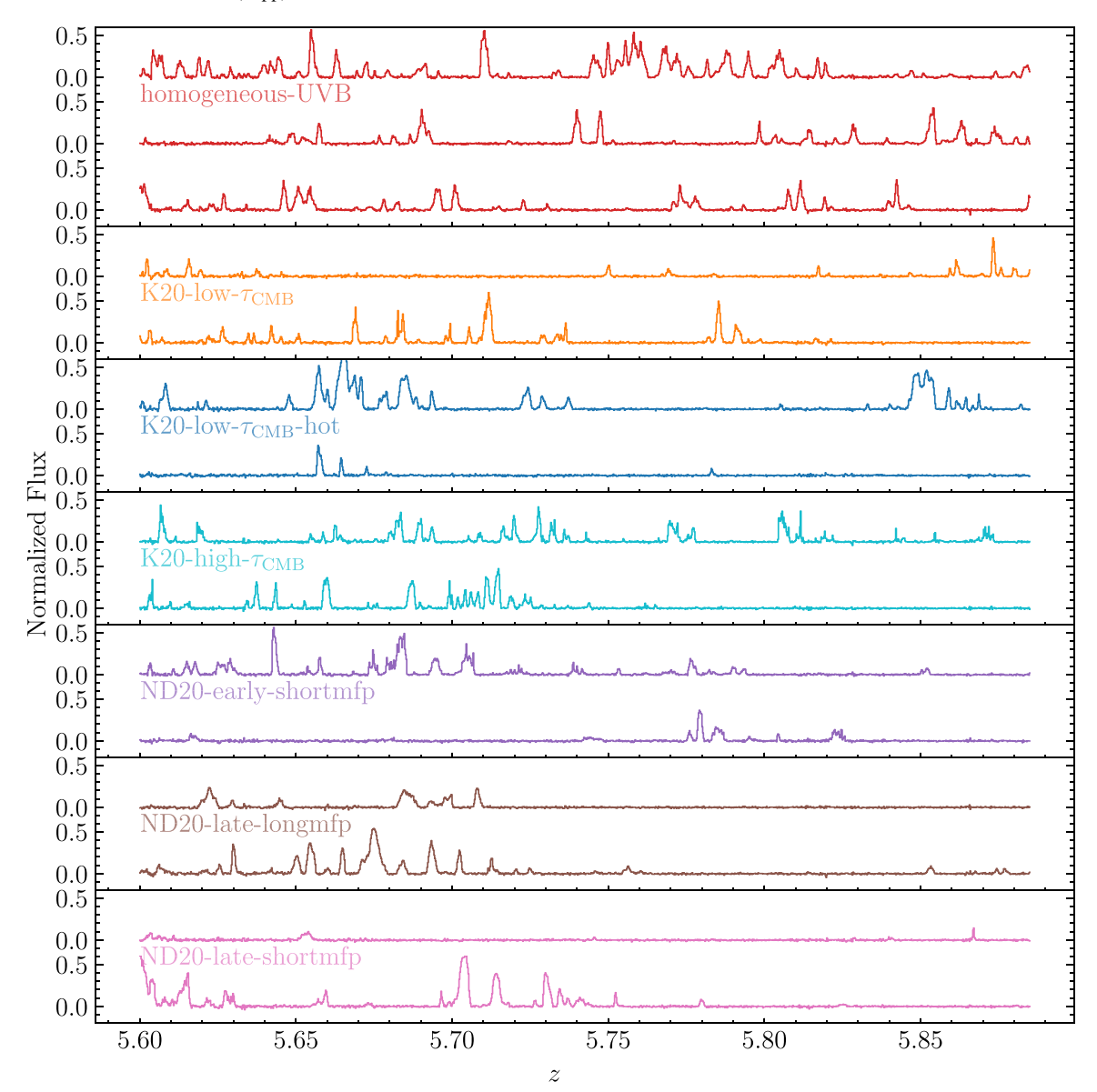


Figure 8. Example mock spectra with binning and S/N chosen to match the Ly $\alpha$  forest of ULAS J0148+0600. We randomly select mock sightlines from each model here. The colored lines represent the flux arrays.

UVB fluctuations also play a significant role in producing the dark gaps in the late reionization models.

#### 5. Discussion

# 5.1. Model Comparisons

We now compare our results to predictions from the simulations described in Section 4. Figure 11 plots the dark gap length versus central redshift for representative mock samples drawn from the homogeneous-UVB model and the K20-low- $\tau_{\rm CMB}$  model. Qualitatively, as redshift increases, the homogeneous-UVB model predicts a milder increase in long dark gaps than is seen in either the K20-low- $\tau_{\rm CMB}$  model or the observations (Figure 3). To quantify the differences, we compute the relevant statistics by drawing mock samples from the simulations that match our observed QSO spectra in redshift and S/N ratio. We then compute the dark gap statistics described in Section 3. We repeat this process 10,000 times for each model and compute the mean,

68% limit, and 95% limit on the expected scatter for the present sample size. Figure 12 compares  $F_{30}$  predicted by models to that calculated from data. The jagged edges of the simulation confidence intervals are caused by the combined effects of step changes in the number of sightlines with redshift and the quantization of  $F_{30}$  for a finite sample size.

The top left panel shows that the homogeneous-UVB model is highly inconsistent with the observations over  $5.3 \lesssim z \lesssim 5.9$ . At  $z \sim 5.8$ , the homogeneous-UVB model under-predicts  $F_{30}$  by a factor of 3. At  $z \sim 5.4$  and over  $5.5 \lesssim z \lesssim 5.8$ , this model is rejected by the data with > 99.9% confidence.

On the other hand, the K20-low- $\tau_{\rm CMB}$  and K20-low- $\tau_{\rm CMB}$ -hot models, wherein reionization ends at  $z\simeq 5.3$ , produce  $F_{30}$  results that are generally consistent with the observations over 5 < z < 6. One exception is that these models underpredict the small number of long dark gaps observed at  $z\sim 5.4$ . The K20-high- $\tau_{\rm CMB}$  model is consistent with the observations at  $z\geqslant 5.75$  but underpredicts  $F_{30}$  at lower redshifts.

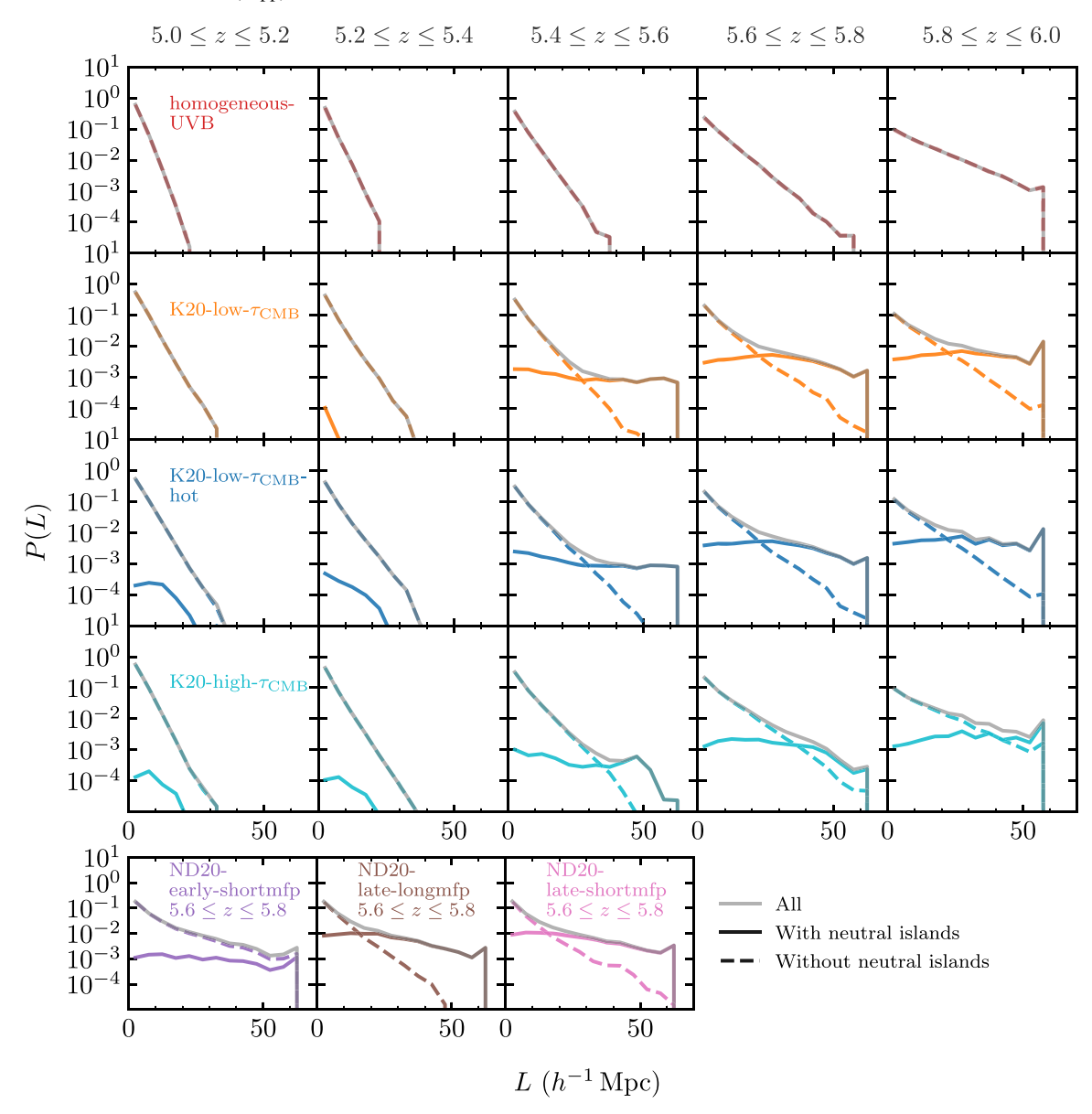


Figure 9. Distribution of dark gaps with and without neutral hydrogen predicted by simulations. A dark gap is considered to contain neutral gas if any pixels inside this gap have a neutral fraction of  $x_{\rm HI} > 0.9$ . P(L) is calculated with count of dark gaps over  $\Delta L = 5h^{-1}$  Mpc bins divided by the total count of dark gaps. The distribution is calculated with dark gaps detected in 10,000 sets of mock spectra (Section 4.4) for each simulation, but with no noise added. We note that the volume neutral fraction information of Nasir & D'Aloisio (2020) models is only available at z = 5.6 and 5.8. The plots for ND20 models are therefore not extended to z = 6.0.

This is a natural consequence of the earlier reionization in this model, which leads to a lower neutral hydrogen fraction and smaller UVB fluctuations at these redshifts.

As shown in the right panels,  $F_{30}$  values from the Nasir & D'Aloisio (2020) models are consistent with the observations within their 95% limits over the available redshift range. Among the ND20 models, ND20-early-shortmfp gives lower  $F_{30}$  values compared to ND20-late, but the difference is within the 68% range for the present sample size.

We compare the cumulative distributions of dark gap length in Figure 13, and give the differences between the observation and the model predictions in Figure 14. In order to facilitate a direct comparison between the observations and simulations, we divide the data into redshift bins of  $\Delta z = 0.2$ . Here, dark gaps extending beyond the boundaries of a redshift bin are truncated at the edge when calculating P(<L) for both the observation and models. Similar to our approach in Section 4.5,

we do this to avoid artifacts from the finite length of the mock spectra.

We present numerical convergence tests for the homogeneous-UVB model in Appendix A. We find that the results for both  $F_{30}$  and P(< L) are relatively insensitive to box size, but that the number of small gaps increases with increasing mass resolution. The impact of mass resolution is more significant for P(< L) at smaller gap lengths than for  $F_{30}$ . For P(< L) measured from the homogeneous-UVB model, therefore, we display predictions based on a higher-resolution run with  $2 \times 2048^3$  particles and a box size of  $L = 40h^{-1}$  Mpc (hereafter  $40_2048$ ) instead of the fiducial configuration of  $2 \times 2048^3$  particles and box size of  $L = 160h^{-1}$  Mpc (hereafter  $160_2048$ ). Because Keating et al. (2020a) use postprocessed radiative transfer simulations, and Nasir & D'Aloisio (2020) simulations are based on an Eulerian code instead of a SPH code, mass resolution effects

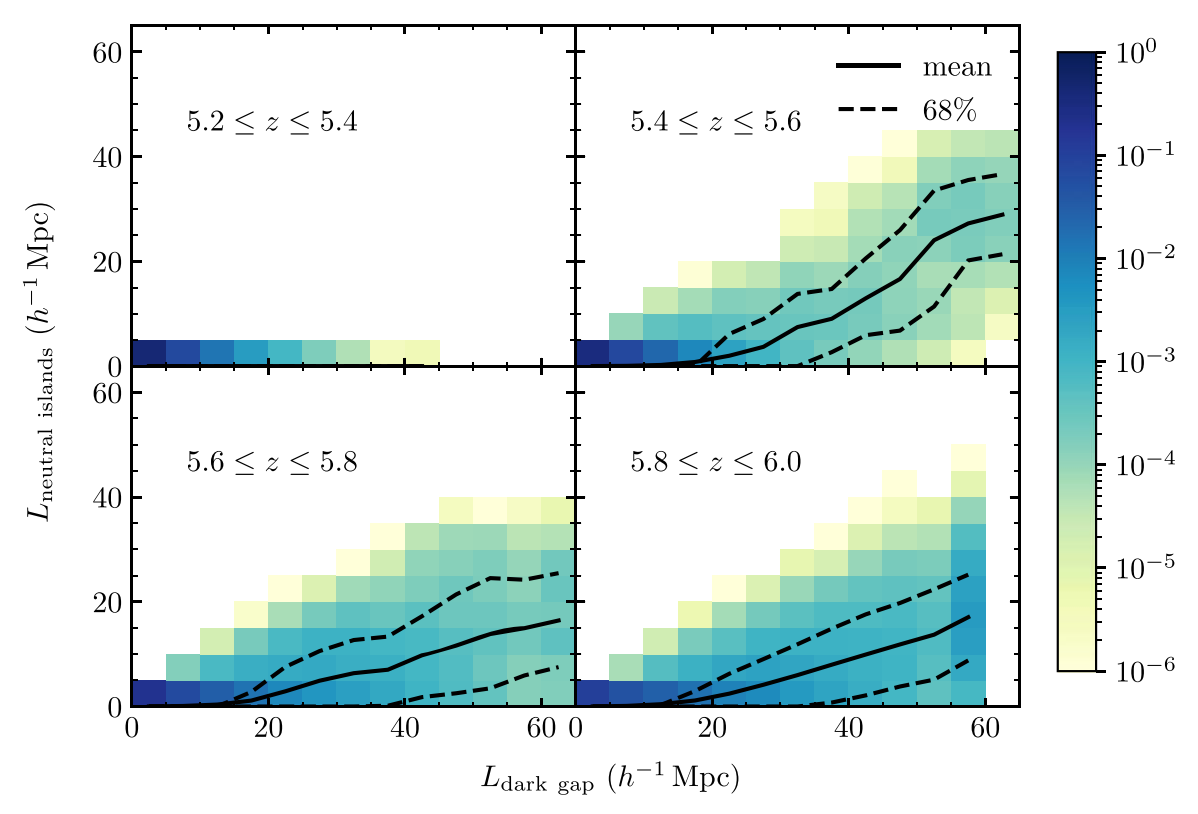


Figure 10. Correlation between neutral islands coverage and dark gap length in the K20-low- $\tau_{CMB}$  model based on 10,000 realizations. The histogram is calculated on 5 × 5 (  $h^{-1}$  Mpc)<sup>2</sup> bins with color indicating the normalized probability, and all dark gaps are included regardless of whether they contain neutral gas. Solid and dashed lines show the mean and 68% interval of the neutral islands coverage.

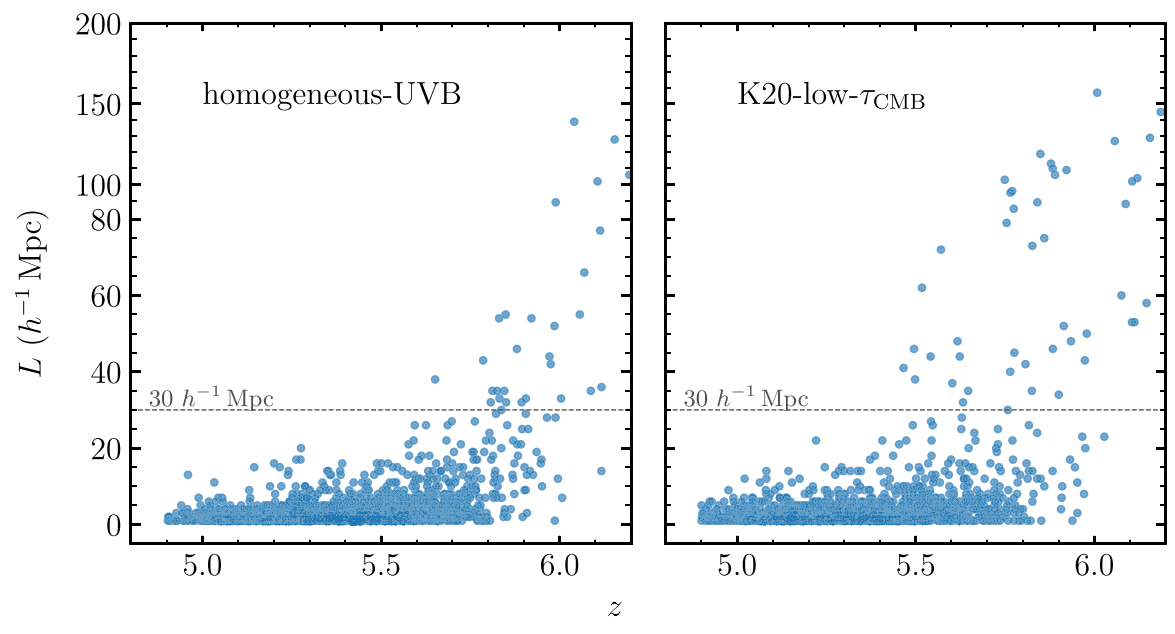


Figure 11. Gap length vs. central redshift for dark gaps detected in mock spectra. For both models, the results shown here are based on one randomly selected set of mock spectra that matches our QSO sample in redshift and S/N ratio.

may be significantly different for these models than for the homogeneous-UVB model. We therefore present results as they are, although mass resolution corrections may be needed.

Over z = 5.6–6.0, the homogeneous-UVB model predicts significantly fewer long gaps than are observed in the data. The discrepancies between the data and the homogeneous-UVB model persist down to the z = 5.2–5.4 bin.

In contrast, the late reionization models, K20-low- $\tau_{\rm CMB}$ , K20-low- $\tau_{\rm CMB}$ -hot, and K20-high- $\tau_{\rm CMB}$ , predict P(<L) values that are generally consistent with the data. Nevertheless, over z=5.7-5.9, we note that these models, especially the K20-high- $\tau_{\rm CMB}$  model, systematically yield higher P(<L), i.e., fewer long gaps, than the observed for some L, though the discrepancies are less conspicuous compared to those for the homogeneous-UVB. At lower

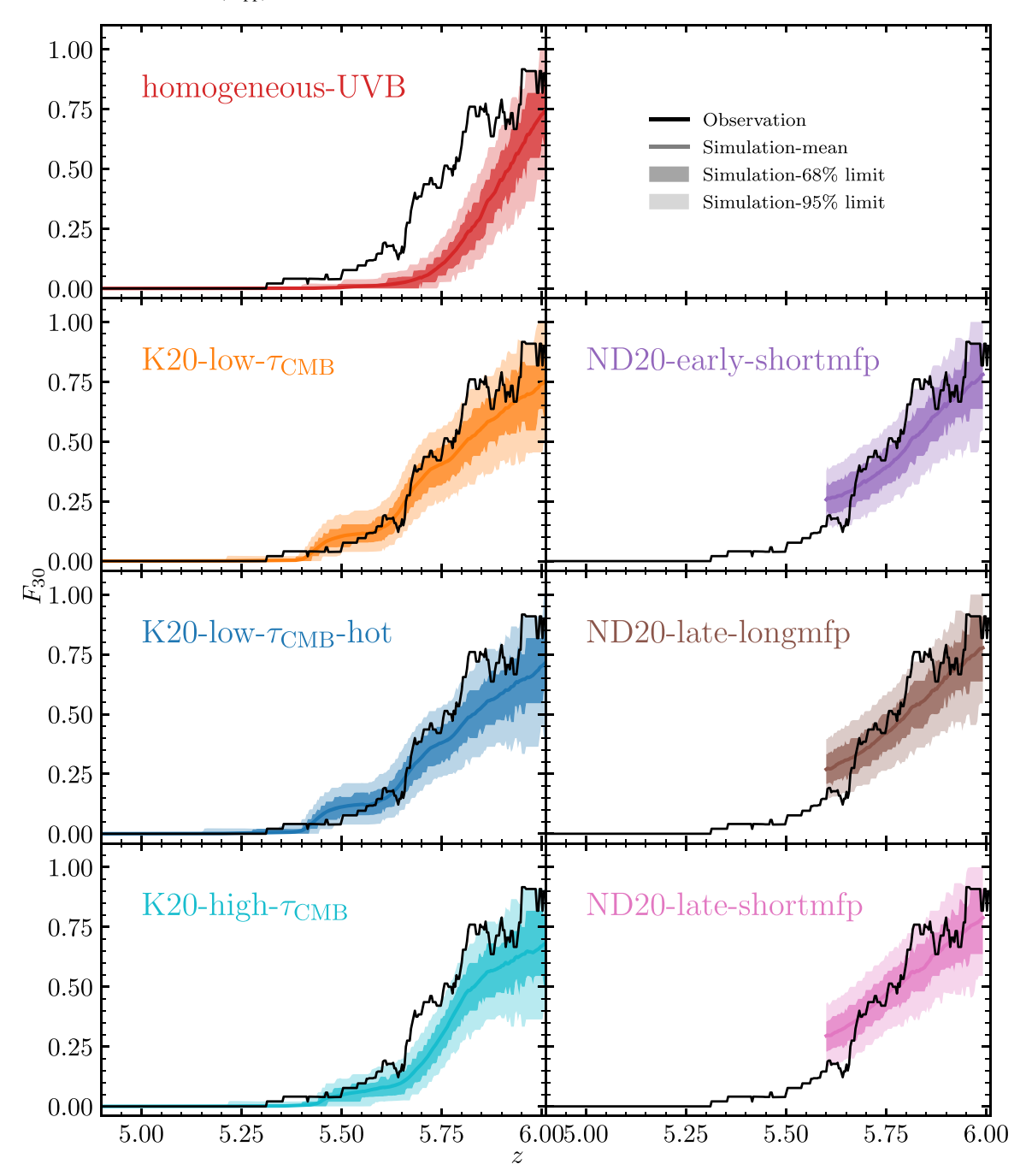


Figure 12. The fraction of sightlines located in dark gaps with  $L \ge 30h^{-1}$  Mpc as a function of redshift. Both the observations (solid black line) and simulations (colored solid line and shaded regions) include gaps that are truncated at the red end of the Ly $\alpha$  forest. Note that we discard dark gaps that are entirely in the 7 pMpc proximity zone and/or in the buffer zone that covers  $30h^{-1}$  Mpc blueward the proximity zone cut. Dark and light shaded regions show the 68% and 95% intervals, respectively, spanned by the models.

redshifts, there are minor differences between the K20 models and the observation. The ND20-early-shortmfp and ND20-late models are generally consistent with the observation in the redshift range  $(5.6\leqslant z\leqslant 6.0)$  currently probed by the simulations.

# 5.2. Implications for Reionization

Combining the results for  $F_{30}$  and P(< L), it is evident that a fully ionized IGM with a homogeneous UV background is disfavored by the observations down to  $z \sim 5.3$ . This result is consistent with the large-scale inhomogeneities in IGM Ly $\alpha$ 

opacity seen in recent  $\tau_{\rm eff}$  measurements (Becker et al. 2015; Bosman et al. 2018; Eilers et al. 2018; Yang et al. 2020b; Bosman et al. 2021a). Our results also agree with the early indication from Gnedin et al. (2017) that models, wherein reionization ended well before z=6, struggled to produce enough long dark gaps.

The late reionization models from Keating et al. (2020a) and Nasir & D'Aloisio (2020) are generally consistent with dark gap statistics in the Ly $\alpha$  forest. In these models, the residual neutral islands at z < 6 coupled with UVB fluctuations can naturally explain the appearance of long dark gaps in the Ly $\alpha$  forest. Among these models, the data tend to prefer those with

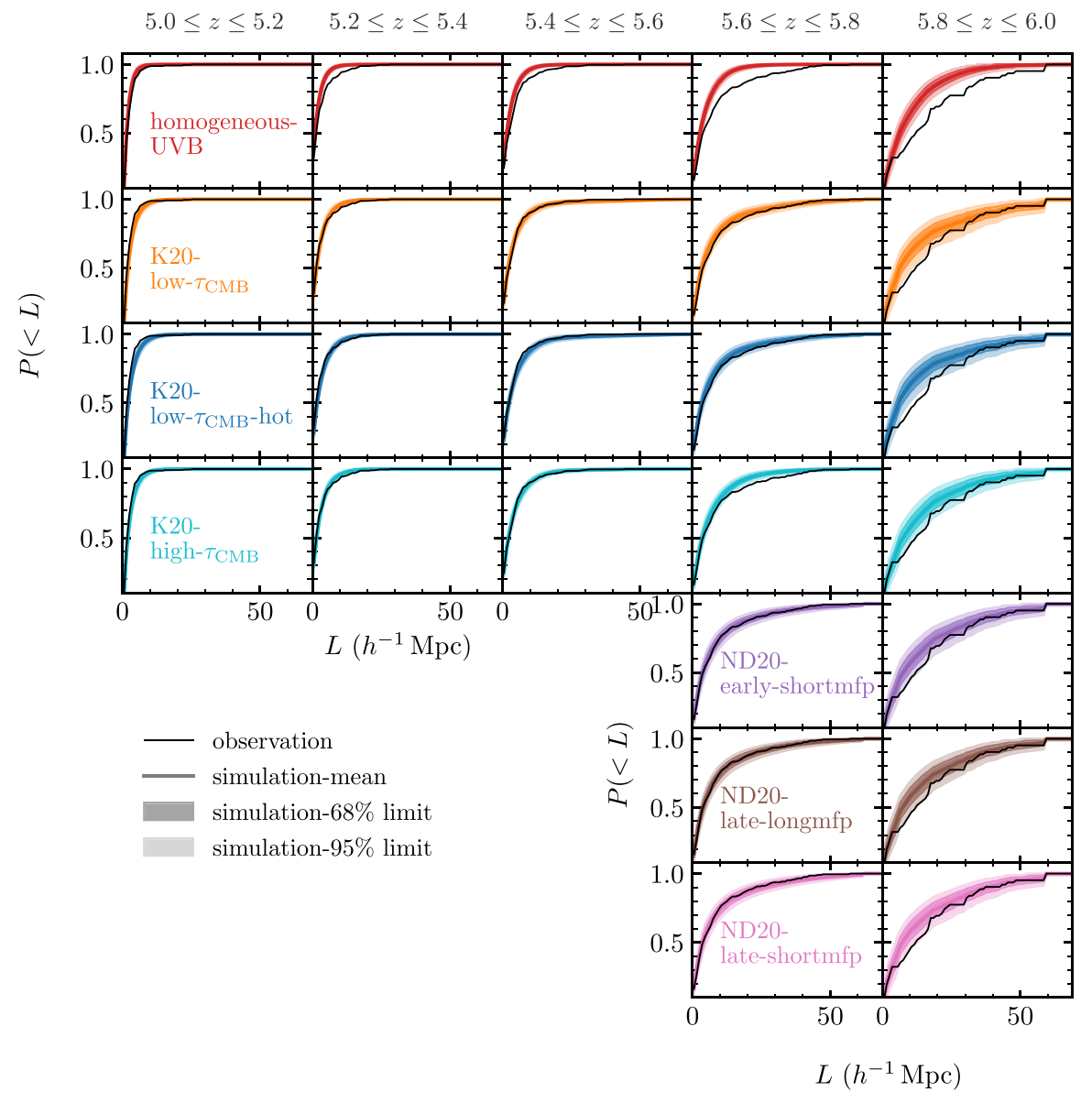


Figure 13. Cumulative distributions of dark gap length. In each redshift bin, the black line shows P(< L) of the observed dark gaps. Dark gaps extending beyond the boundaries of the  $\Delta z = 0.2$  window are truncated at the edge. The colored lines and dark/light-shaded regions represent the mean and 68%/95% limits, respectively, of P(< L) in mock samples drawn from the models. In this figure, we use a high-mass-resolution run from the Sherwood Simulation Suite (Bolton et al. 2017) for the homogeneous-UVB model instead of the fiducial configuration. See text for details.

later and more rapid reionization histories. For example, the K20-low- $\tau_{\rm CMB}$  and K20-low- $\tau_{\rm CMB}$ -hot models, which have a reionization midpoint of  $z_{50}=6.7$ , is somewhat more consistent (see curves and shades near  $5.6\leqslant z \leqslant 5.8$  in Figures 12, 13, and 14) with the dark gap statistics at z<6 than the K20-high- $\tau_{\rm CMB}$  mode, for which  $z_{50}=8.4$ . A late and rapid reionization is also suggested by the recent mean free path measurement from Becker et al. (2021) (see also Cain et al. 2021; Davies et al. 2021).

Alternatively, long dark gaps can arise from a fully reionized IGM provided that there are large UVB fluctuations. The early reionization model from Nasir & D'Aloisio (2020), which retains postreionization fluctuations in the UV background and IGM temperature, is consistent with the data over at least 5.6 < z < 6.0, where the available simulation outputs allow mock spectra to be compared to the data using the methods described above. Extending these simulations down to lower

redshifts would be helpful for testing the pure fluctuating UVB model further.

#### 6. Summary

In this paper, we present a search for dark gaps in the Ly $\alpha$  forest over 5 < z < 6. We use high-S/N spectra of 55 QSOs at  $z_{\rm em} > 5.5$  taken with Keck ESI and VLT X-Shooter, including data from the new XQR-30 VLT Large Programme. We focus on two statistics: the fraction of sightlines containing dark gaps of length  $L \geqslant 30h^{-1}$  Mpc as a function of redshift,  $F_{30}$ , which we introduce here for the first time, and the dark gap length distribution, P(< L). Our primary goal is to quantify the persistence of large Ly $\alpha$ -opaque regions in the IGM below redshift six, and to evaluate the consistency between the observed dark gap statistics and predictions from various models. We include a model with a fully ionized IGM and a uniform ionizing UV background, and others with large islands

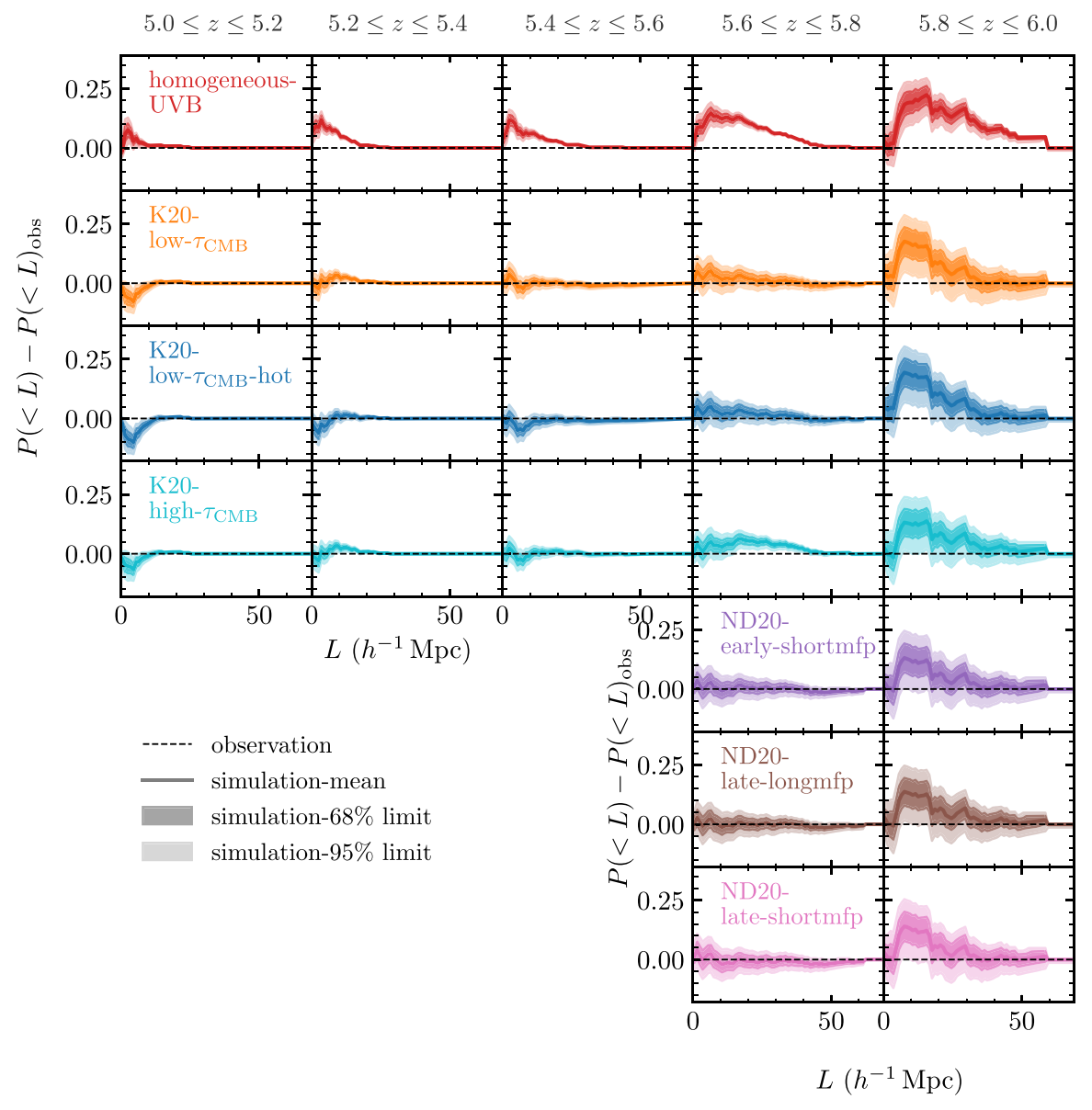


Figure 14. Similar to Figure 13, but showing the differences on cumulative distributions of dark gap length between the models and the observations.

of neutral gas and/or UVB fluctuations. Our main results can be summarized as follows:

- 1. We identify 50 long dark gaps  $(L \geqslant 30h^{-1}\,\mathrm{Mpc})$  in the Ly\$\alpha\$ forest from our sample. Two long dark gaps are found at z < 5.5, with one extending down to  $z \simeq 5.3$ . We also report new ultralong dark gaps  $(L > 80h^{-1}\,\mathrm{Mpc})$  below z = 6, similar to the one previously reported toward ULAS J0148+0600 by Becker et al. (2015). The presence of long dark gaps at these redshifts demonstrates that large regions of the IGM remain opaque to Ly\$\alpha\$ down to  $z \simeq 5.3$ .
- 2. In terms of both  $F_{30}$  and P(<L), a fully ionized IGM with a homogeneous UVB is disfavored by the data down to  $z \simeq 5.3$ .
- 3. Models wherein reionization ends significantly below redshift six (Keating et al. 2020a; Nasir & D'Aloisio 2020) are broadly consistent with the data. Among these, the data favor models with a reionization midpoint near  $z \sim 7$  and an end at  $z \simeq 5.3$  or later. In these models,

- dark gaps arise from a combination of neutral patches in the IGM and regions of low ionizing UV background, which are often adjacent to one another.
- 4. We also find consistency with a model wherein reionization ends by z = 6 but the IGM retains large fluctuations in the UV background (Nasir & D'Aloisio 2020), at least over 5.6 < z < 6.0.

Overall, the evolution of dark gaps observed at z < 6 suggests that signatures of reionization remain present in the IGM until at least  $z \simeq 5.3$  in the form of neutral hydrogen islands and/or fluctuations in the ionizing UV background. We note that this work focuses on dark gaps in the Ly $\alpha$  forest. Given its lower optical depth, however, Ly $\beta$  may also be a useful tool. For example, islands of neutral gas may tend to produce more long Ly $\beta$  troughs than are created by fluctuations in the UV background (e.g., Nasir & D'Aloisio 2020). These and other statistics should provide further details on how the IGM evolves near the end of reionization.

We thank Elisa Boera and Fahad Nasir for their help and useful discussion. We also thank the anonymous reviewer for their careful reading of the paper and thoughtful comments.

Y.Z., G.D.B., and H.M.C. were supported by the National Science Foundation through grants AST-1615814 and AST-1751404. H.M.C. was also supported by the National Science Foundation Graduate Research Fellowship Program under grant No. DGE-1326120. S.E.I.B. acknowledges funding from the European Research Council (ERC) under the European Union's Horizon 2020 research and innovation program (grant agreement No. 740246 "Cosmic Gas"). L.C.K. was supported by the European Union's Horizon 2020 research and innovation program under the Marie Skłodowska-Curie grant agreement No. 885990. F.B. acknowledges support from the Australian Research Council through Discovery Projects (award DP190100252) and Chinese Academy of Sciences (CAS) through a China-Chile Joint Research Fund (CCJRF1809) administered by the CAS South America Center for Astronomy (CASSACA). A.-C.E. acknowledges support by NASA through the NASA Hubble Fellowship grant # HF2-51434 awarded by the Space Telescope Science Institute, which is operated by the Association of Universities for Research in Astronomy, Inc., for NASA, under contract NAS5-26555. X.F. and J.Y. acknowledge support from the NSF grants AST 15-15115 and AST 19-08284. M.G.H. acknowledges support from the UKRI STFC (grant Nos. ST/N000927/ 1 and ST/S000623/1). G.K.'s research is partly supported by the Max Planck Society via a partner group grant. A.P. acknowledges support from the ERC Advanced Grant INTERSTELLAR H2020/740120. Parts of this work was supported by the Australian Research Council Centre of Excellence for All Sky Astrophysics in 3 Dimensions (ASTRO 3D), through project # CE170100013. F.W. thanks the support provided by NASA through the NASA Hubble Fellowship grant #HST-HF2-51448.001-A awarded by the Space Telescope Science Institute, which is operated by the Association of Universities for Research in Astronomy, Incorporated, under NASA contract NAS5-26555.

Based on observations collected at the European Southern Observatory under ESO programmes 060.A-9024(A), 084.A-0360(A), 084.A-0390(A), 084.A-0550(A), 085.A-0299(A), 086.A-0162(A), 086.A-0574(A), 087.A-0607(A), 088.A-0897 (A), 091.C-0934(B), 096.A-0095(A), 096.A-0418(A), 097.B-1070(A), 098.A-0111(A), 098.B-0537(A), 0100.A-0243(A), 0100.A-0625(A), 0101.B-0272(A), 0102.A-0154(A), 0102.A-0478(A), 1103.A-0817(A), and 1103.A-0817(B).

Some of the data presented herein were obtained at the W. M. Keck Observatory, which is operated as a scientific partnership among the California Institute of Technology, the University of California and the National Aeronautics and Space Administration. The Observatory was made possible by the generous financial support of the W. M. Keck Foundation. The authors wish to recognize and acknowledge the very significant cultural role and reverence that the summit of Maunakea has always had within the indigenous Hawaiian community. We are most fortunate to have the opportunity to conduct observations from this mountain. Finally, this research has made use of the Keck Observatory Archive (KOA), which is operated by the W.M. Keck Observatory and the NASA

Exoplanet Science Institute (NExScI), under contract with the National Aeronautics and Space Administration.

This work was performed using the Cambridge Service for Data Driven Discovery (CSD3), part of which is operated by the University of Cambridge Research Computing on behalf of the STFC DiRAC HPC Facility (www.dirac.ac.uk). The DiRAC component of CSD3 was funded by BEIS capital funding via STFC capital grants ST/P002307/1 and ST/R002452/1 and STFC operations grant ST/R00689X/1. This work further used the DiRAC@Durham facility managed by the Institute for Computational Cosmology on behalf of the STFC DiRAC HPC Facility. The equipment was funded by BEIS capital funding via STFC capital grants ST/P002293/1 and ST/R002371/1, Durham University and STFC operations grant ST/R000832/1. DiRAC is part of the National e-Infrastructure.

Facilities: Keck:II (ESI), VLT:Kueyen (X-Shooter).

Software: Astropy (Astropy Collaboration et al. 2013, 2018), Matplotlib (Hunter 2007), NumPy (Harris et al. 2020), SpectRes (Carnall 2017).

#### Appendix A Numerical Convergence

Here we test the convergence of our results for the homogeneous-UVB model with different box sizes and mass resolutions. We denote different simulation configurations as X\_Y, where X is the box size in comoving Mpc  $h^{-1}$  and Y = [(number of dark matter + baryon particles)/2]<sup>1/3</sup>. The fiducial configuration used in Section 3 is 160\_2048.

To calculate  $F_{30}$  with smaller boxes, we first stitch the short skewers to form 160 Mpc/h skewers, and then create mock spectra following the method described in Section 4.4. In Figure A1, we compare  $F_{30}$  for mock data generated from different simulation configurations. We find little dependence on box size.  $F_{30}$  decreases slightly with increasing mass resolution, though the differences are within the expected 68% scatter for the present sample size. We compare P(< L) with different configurations to the baseline configurations by calculating  $P(\langle L) - P(\langle L)_{\text{baseline}}$  in Figure A2. For a fixed mass resolution and varying box size, we compare simulations to our fiducial 160\_2048 simulation. For a fixed box size but varying mass resolution, we compare simulations to the 40\_512 configuration, which has the same mass resolution of 160\_2048. Similar to  $F_{30}$ , the variations in P(< L) with box size are relatively minor. The impact of mass resolution is more significant, especially for smaller L.

Figures A1 and A2 suggest that mass resolution has a larger impact than box size on our statistics, in the sense that simulations with lower mass resolutions tend to produce more long gaps and fewer short gaps. This is because weak, narrow Ly $\alpha$  transmission peaks tend to be suppressed at lower resolution. This effect may need to be considered for larger samples. We emphasize that the homogeneous-UVB models that we are using for these convergence tests contain significantly fewer long gaps than the late reionization and fluctuating UVB models. It is therefore unclear how well the trends we see for large L would apply to these models, although it is likely that the effects of mass resolution we see at smaller gap lengths would generally be present in SPH simulations.

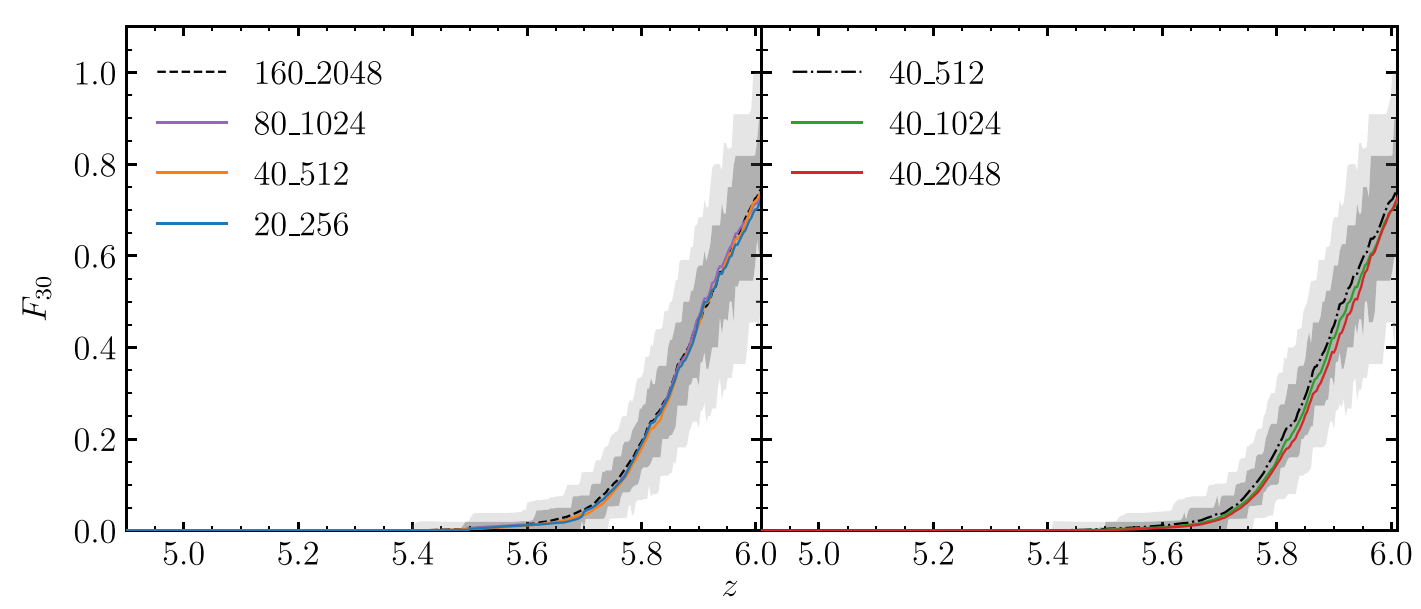
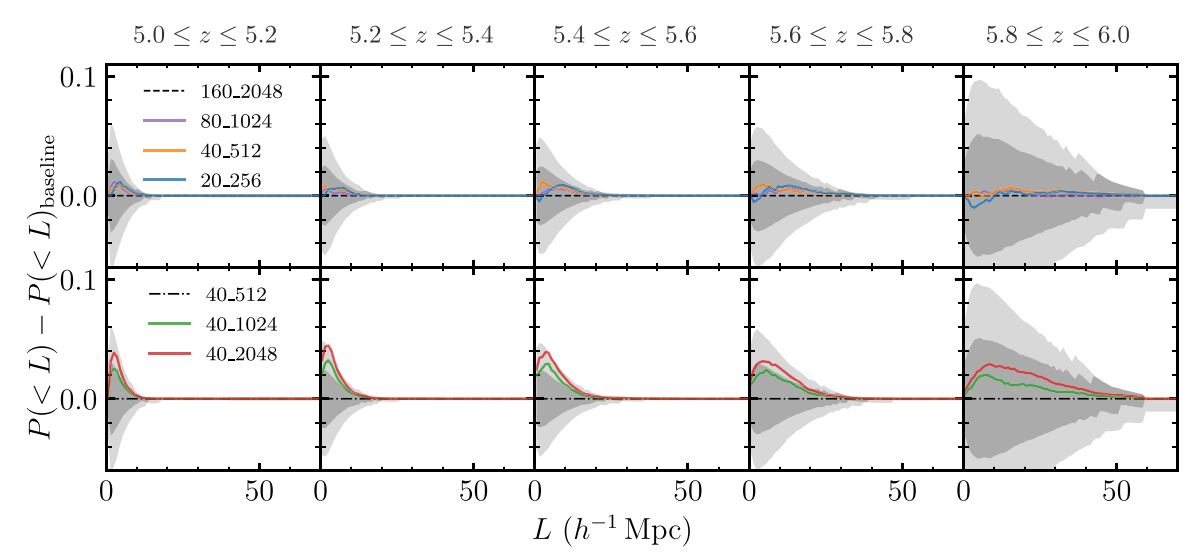


Figure A1. Fractions of QSO spectra exhibiting long ( $L \ge 30h^{-1}$  Mpc) dark gaps as a function of redshift with different simulation configurations. The left panel compares results for varying box sizes but fixed mass resolution. The dark gray and light gray shaded regions are the 68% and 95% limits on the expected scatter for the present sample size from the  $160\_2048$  simulation, which are the same as the shaded regions in Figure 12. The right panel compares results for varying mass resolutions but fixed box size. The dashed–dotted line is the mean, and shaded regions are 68% and 95% limits of the prediction from the  $40\_512$  simulation.



**Figure A2.** Difference on dark gap length distributions for different box sizes and mass resolutions compared to the baseline configurations. The top and bottom rows compare results for varying box sizes and varying mass resolutions, respectively. The dark gray and light gray shaded regions are the 68% and 95% limits on the expected scatter for the present sample size from the 160\_2048 simulation (Top panel) and from the 40\_512 simulation (Bottom panel).

# Appendix B Simulation Predictions without Masking

For consistency with the observations, we mask out small wavelength regions in the mock spectra that coincide with peaks in the observed flux error arrays, as described in Section 3.1.

Figure B1 shows how the simulation results change without masking. The model predictions for  $F_{30}$  decrease because the masks sometimes fall on transmission peaks. The overall impact is minor; however, we emphasize that the observations should be compared to the simulation results with masking included.

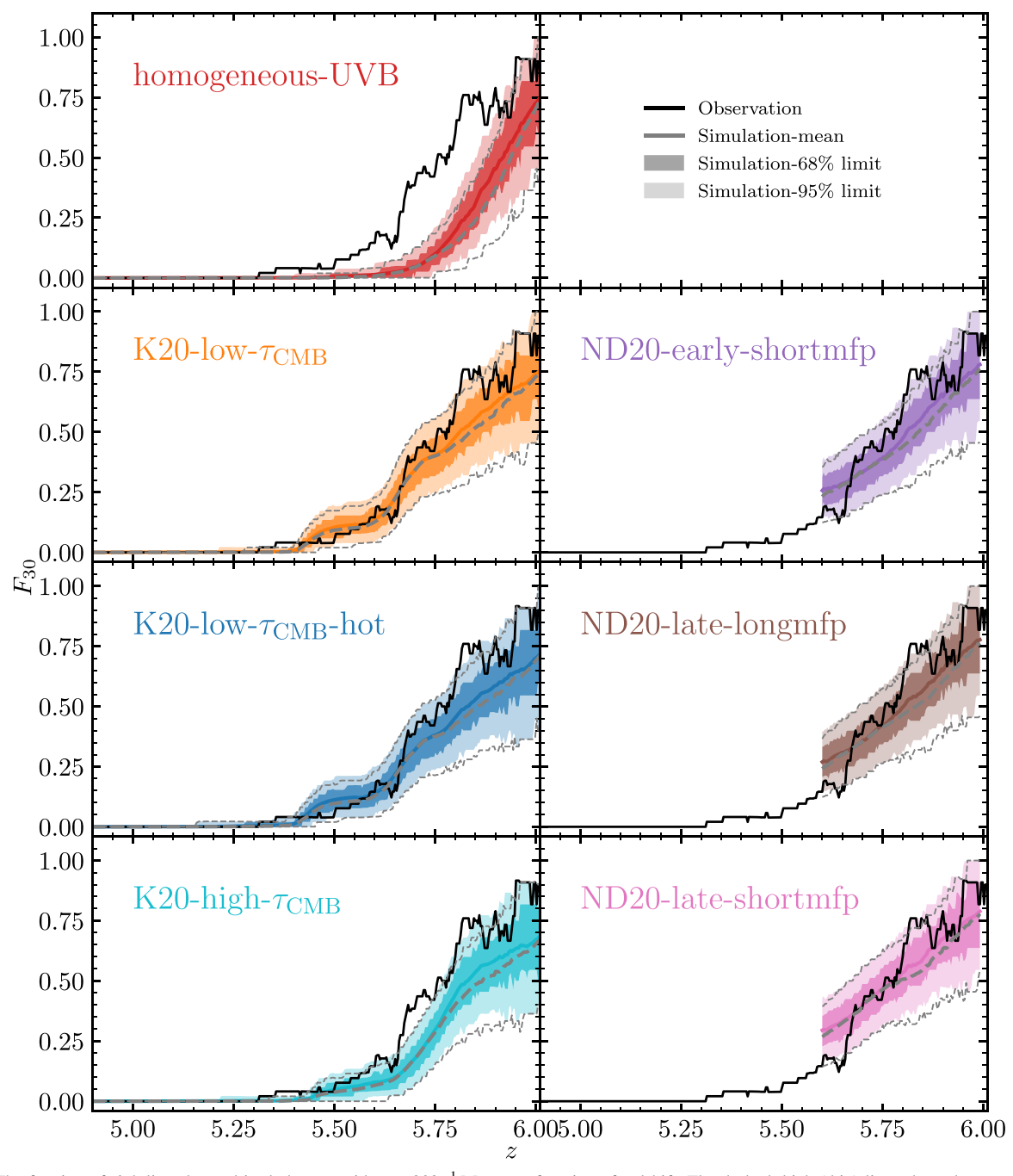
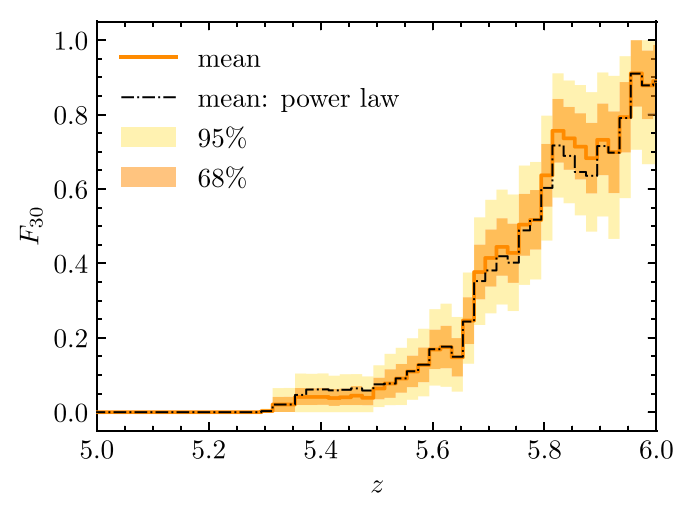


Figure B1. The fraction of sightlines located in dark gaps with  $L \ge 30h^{-1}$  Mpc as a function of redshift. The dashed thick (thin) lines show the mean values (95% range) of simulation predictions without masking regions in the mock spectra that coincide with peaks in the flux error array. Other lines and shaded regions are as described in Figure 12.



**Figure C1.** Measured fraction of QSO spectra exhibiting long  $(L \ge 30h^{-1} \text{ Mpc})$  dark gaps as a function of redshift. The dotted–dashed line shows the result based on the power law continuum fitting. Other lines and regions are as described in Figure 5.

# Appendix C $F_{30}$ Based on the Power-law Continuum Fitting

For reference, in this section, we calculate  $F_{30}$  based on the power-law continuum fitting. The power-law continua are in the form of  $a\lambda^{-b}$ , with a and b being free parameters. We

generally estimate the power-law continua over  $\sim 1285-1350\,\text{Å}$  in the rest frame, which is relatively free of emission lines, and we extend the fitting range out to  $\sim 2000\,\text{Å}$  when possible. Figure C1 compares the results. The consistency (within  $1\sigma$ ) between  $F_{30}$  based on the PCA continuum and power law continuum suggests that our results are insensitive to continuum-fitting methods.

# Appendix D Effect of Metal Absorbers on $F_{30}$

The strong HI absorption typically associated with metal systems may potentially impact the observed  $F_{30}$  by connecting otherwise shorter gaps. We test whether this effect could be significant by dividing dark gaps at the redshifts of DLAs and other metal systems. We also exclude a 3000 km s<sup>-1</sup> region surrounding the redshift of the metal absorber in order to allow for extended DLA absorption and/or strong absorbers clustered around the metal system. As shown in Figure D1, the impact on  $F_{30}$  is relativel minor, with a maximum decrease of  $\sim 0.1$  at  $z \sim 5.8$ . We caution that list of metal absorbers used here may be incomplete; however, we have verified that the three long dark gaps at  $z \lesssim 5.5$  in particular do not contain metals to within the sensitivity of our data. In summary, we find that the impact of metal systems on  $F_{30}$  in this regard is minor, and that the homogenous-UVB model is strongly ruled out regardless of how these systems are treated.

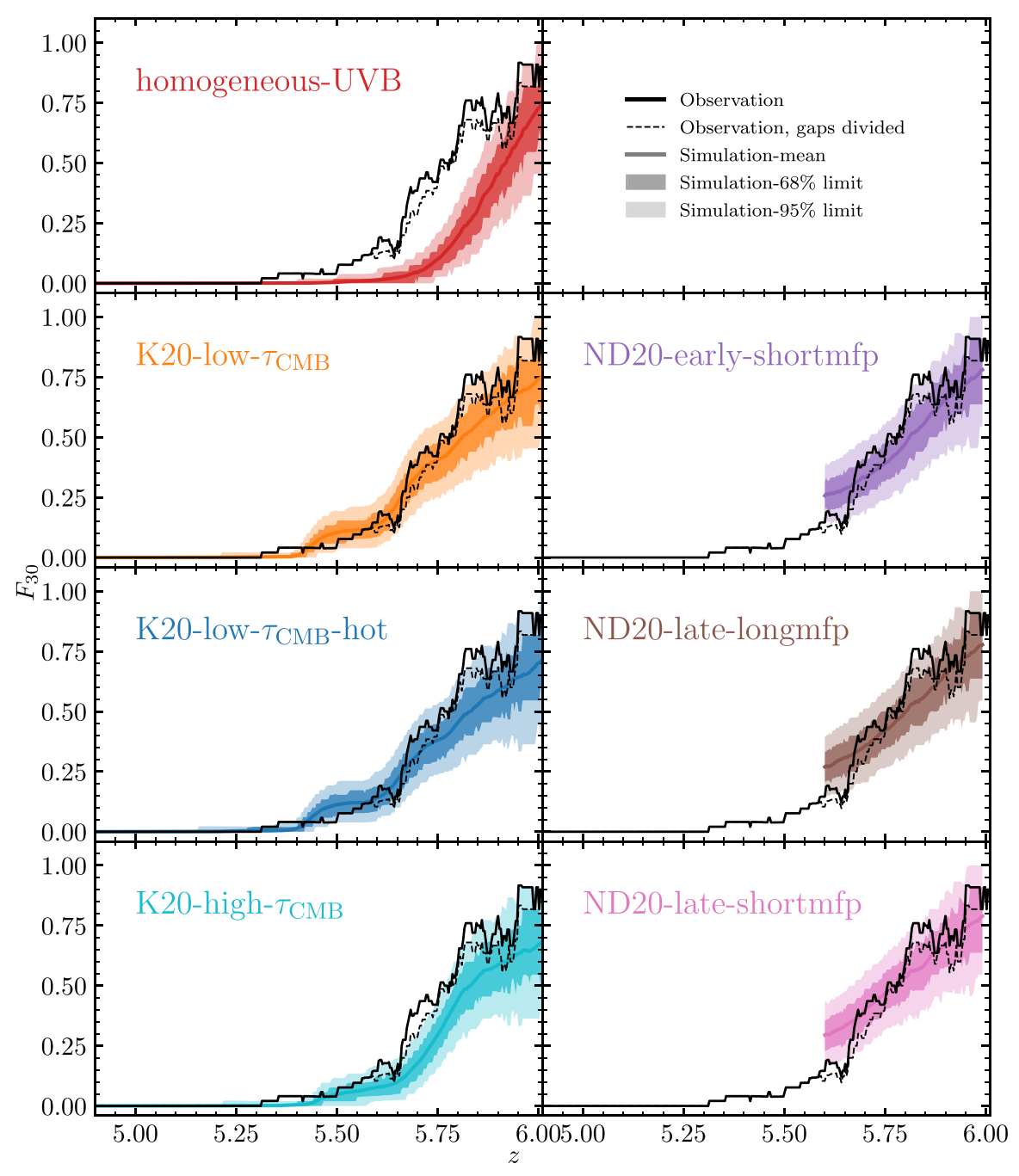


Figure D1. The fraction of sightlines located in dark gaps with  $L \ge 30h^{-1}$  Mpc as a function of redshift. The dashed lines show  $F_{30}$  from observations with dark gaps divided at the redshifts of DLAs or metal systems with a 3000 km s<sup>-1</sup> interval. Other lines and shaded regions are as described in Figure 12.

# ORCID iDs

Yongda Zhu https://orcid.org/0000-0003-3307-7525
George D. Becker https://orcid.org/0000-0003-2344-263X
Sarah E. I. Bosman https://orcid.org/0000-0001-8582-7012
Laura C. Keating https://orcid.org/0000-0001-5211-1958
Holly M. Christenson https://orcid.org/0000-0002-0421-065X
Eduardo Bañados https://orcid.org/0000-0002-2931-7824
Fuyan Bian https://orcid.org/0000-0002-1620-0897
Frederick B. Davies https://orcid.org/0000-0003-0821-3644
Valentina D'Odorico https://orcid.org/0000-0003-3693-3091
Anna-Christina Eilers https://orcid.org/0000-0003-2895-6218
Xiaohui Fan https://orcid.org/0000-0003-3310-0131

Martin G. Haehnelt https://orcid.org/0000-0001-8443-2393 Girish Kulkarni https://orcid.org/0000-0001-5829-4716 Andrea Pallottini https://orcid.org/0000-0002-7129-5761 Yuxiang Qin https://orcid.org/0000-0002-4314-1810 Feige Wang https://orcid.org/0000-0002-7633-431X Jinyi Yang https://orcid.org/0000-0001-5287-4242

# References

Astropy Collaboration, Price-Whelan, A. M., Sipőcz, B. M., et al. 2018, AJ, 156, 123

Astropy Collaboration, Robitaille, T. P., Tollerud, E. J., et al. 2013, A&A, 558, A33

```
Aubert, D., & Teyssier, R. 2008, MNRAS, 387, 295
Aubert, D., & Teyssier, R. 2010, ApJ, 724, 244
Bañados, E., Decarli, R., Walter, F., et al. 2015, ApJL, 805, L8
Bañados, E., Venemans, B. P., Mazzucchelli, C., et al. 2018, Natur, 553, 473
Barnett, R., Warren, S. J., Becker, G. D., et al. 2017, A&A, 601, A16
Becker, G. D., Bolton, J. S., Madau, P., et al. 2015, MNRAS, 447, 3402
Becker, G. D., D'Aloisio, A., Christenson, H. M., et al. 2021, MNRAS,
   508, 1853
Becker, G. D., Davies, F. B., Furlanetto, S. R., et al. 2018, ApJ, 863, 92
Becker, G. D., Pettini, M., Rafelski, M., et al. 2019, ApJ, 883, 163
Boera, E., Becker, G. D., Bolton, J. S., & Nasir, F. 2019, ApJ, 872, 101
Bolton, J. S., Puchwein, E., Sijacki, D., et al. 2017, MNRAS, 464, 897
Bosman, S. E. I., Davies, F. B., Becker, G. D., et al. 2021a, arXiv:2108.03699
Bosman, S. E. I., Ďurovčíková, D., Davies, F. B., & Eilers, A. C. 2021b,
   MNRAS, 503, 2077
Bosman, S. E. I., Fan, X., Jiang, L., et al. 2018, MNRAS, 479, 1055
Bromm, V., & Larson, R. B. 2004, ARA&A, 42, 79
Cain, C., D'Aloisio, A., Gangolli, N., & Becker, G. D. 2021, ApJL, 917, L37
Carilli, C. L., Neri, R., Wang, R., et al. 2007, ApJ, 666, L9
Carnall, A. C. 2017, arXiv:1705.05165
Chardin, J., Puchwein, E., & Haehnelt, M. G. 2017, MNRAS, 465, 3429
Chen, S.-F. S., Simcoe, R. A., Torrey, P., et al. 2017, ApJ, 850, 188
Choudhury, T. R., Paranjape, A., & Bosman, S. E. I. 2021, MNRAS, 501, 5782
Christenson, H. M., Becker, G. D., Furlanetto, S. R., et al. 2021, ApJ, 923, 87
D'Aloisio, A., McQuinn, M., & Trac, H. 2015, ApJL, 813, L38
Davies, F. B., Bosman, S. E. I., Furlanetto, S. R., Becker, G. D., &
   D'Aloisio, A. 2021, ApJL, 918, L35
Davies, F. B., & Furlanetto, S. R. 2016, MNRAS, 460, 1328
Davies, F. B., Hennawi, J. F., Bañados, E., et al. 2018a, ApJ, 864, 142
Davies, F. B., Hennawi, J. F., Bañados, E., et al. 2018b, ApJ, 864, 143
Dayal, P., & Ferrara, A. 2018, PhR, 780, 1
de Belsunce, R., Gratton, S., Coulton, W., & Efstathiou, G. 2021, MNRAS,
   507, 1072
Decarli, R., Walter, F., Venemans, B. P., et al. 2018, ApJ, 854, 97
Eilers, A.-C., Davies, F. B., & Hennawi, J. F. 2018, ApJ, 864, 53
Eilers, A.-C., Davies, F. B., Hennawi, J. F., et al. 2017, ApJ, 840, 24
Eilers, A.-C., Hennawi, J. F., Decarli, R., et al. 2020, ApJ, 900, 37
Fan, X., Strauss, M. A., Becker, R. H., et al. 2006, AJ, 132, 117
Furlanetto, S. R., Hernquist, L., & Zaldarriaga, M. 2004, MNRAS, 354, 695
Gaikwad, P., Srianand, R., Haehnelt, M. G., & Choudhury, T. R. 2021,
     NRAS, 506, 4389
Gallerani, S., Ferrara, A., Fan, X., & Choudhury, T. R. 2008, MNRAS,
   386, 359
Gnedin, N. Y., Becker, G. D., & Fan, X. 2017, ApJ, 841, 26
Greig, B., Mesinger, A., & Bañados, E. 2019, MNRAS, 484, 5094
Greig, B., Mesinger, A., Haiman, Z., & Simcoe, R. A. 2017, MNRAS,
   466, 4239
Haardt, F., & Madau, P. 2012, ApJ, 746, 125
```

Harris, C. R., Millman, K. J., van der Walt, S. J., et al. 2020, Natur, 585, 357

```
Hoag, A., Bradač, M., Huang, K., et al. 2019, ApJ, 878, 12
Horne, K. 1986, PASP, 98, 609
Hu, W., Wang, J., Zheng, Z.-Y., et al. 2019, ApJ, 886, 90
Hunter, J. D. 2007, CSE, 9, 90
Jiang, L., Fan, X., Vestergaard, M., et al. 2007, AJ, 134, 1150
Jones, A., Noll, S., Kausch, W., Szyszka, C., & Kimeswenger, S. 2013, A&A,
  560, A91
Jung, I., Finkelstein, S. L., Dickinson, M., et al. 2020, ApJ, 904, 144
Kashino, D., Lilly, S. J., Shibuya, T., Ouchi, M., & Kashikawa, N. 2020, ApJ,
  888. 6
Keating, L. C., Kulkarni, G., Haehnelt, M. G., Chardin, J., & Aubert, D. 2020a,
   MNRAS, 497, 906
Keating, L. C., Weinberger, L. H., Kulkarni, G., et al. 2020b, MNRAS,
  491, 1736
Kelson, D. D. 2003, PASP, 115, 688
Kulkarni, G., Keating, L. C., Haehnelt, M. G., et al. 2019a, MNRAS, 485, L24
Kulkarni, G., Worseck, G., & Hennawi, J. F. 2019b, MNRAS, 488, 1035
Kurk, J. D., Walter, F., Fan, X., et al. 2007, ApJ, 669, 32
Maiolino, R., Cox, P., Caselli, P., et al. 2005, A&A, 440, L51
Mason, C. A., Fontana, A., Treu, T., et al. 2019, MNRAS, 485, 3947
Mason, C. A., Treu, T., Dijkstra, M., et al. 2018, ApJ, 856, 2
Mazzucchelli, C., Bañados, E., Venemans, B. P., et al. 2017, ApJ, 849, 91
McGreer, I. D., Mesinger, A., & D'Odorico, V. 2015, MNRAS, 447, 499
McQuinn, M. 2016, ARA&A, 54, 313
Meiksin, A. 2020, MNRAS, 491, 4884
Nasir, F., & D'Aloisio, A. 2020, MNRAS, 494, 3080
Noll, S., Kausch, W., Barden, M., et al. 2012, A&A, 543, A92
Parsa, S., Dunlop, J. S., & McLure, R. J. 2018, MNRAS, 474, 2904
Paschos, P., & Norman, M. L. 2005, ApJ, 631, 59
Planck Collaboration, Aghanim, N., Akrami, Y., et al. 2020, A&A, 641, A6
Qin, Y., Mesinger, A., Bosman, S. E. I., & Viel, M. 2021, MNRAS, 506,
Sheinis, A. I., Bolte, M., Epps, H. W., et al. 2002, PASP, 114, 851
Shen, Y., Wu, J., Jiang, L., et al. 2019, ApJ, 873, 35
Songaila, A., & Cowie, L. L. 2002, AJ, 123, 2183
Springel, V. 2005, MNRAS, 364, 1105
Trac, H., & Pen, U.-L. 2004, NewA, 9, 443
Venemans, B. P., Walter, F., Neeleman, M., et al. 2020, ApJ, 904, 130
Vernet, J., Dekker, H., D'Odorico, S., et al. 2011, A&A, 536, A105
Walther, M., Oñorbe, J., Hennawi, J. F., & Lukić, Z. 2019, ApJ, 872, 13
Wang, F., Davies, F. B., Yang, J., et al. 2020, ApJ, 896, 23
Wang, F., Fan, X., Yang, J., et al. 2021, ApJ, 908, 53
Wang, F., Wang, R., Fan, X., et al. 2019, ApJ, 880, 2
Wang, R., Carilli, C. L., Neri, R., et al. 2010, ApJ, 714, 699
Wang, R., Wagg, J., Carilli, C. L., et al. 2013, ApJ, 773, 44
Wold, I. G. B., Malhotra, S., Rhoads, J., et al. 2021, arXiv:2105.12191
Yang, J., Venemans, B., Wang, F., et al. 2019, ApJ, 880, 153
Yang, J., Wang, F., Fan, X., et al. 2020a, ApJ, 897, L14
Yang, J., Wang, F., Fan, X., et al. 2020b, ApJ, 904, 26
```